Mechanical Engineering Semester Project

Fluidic design of Liquid Oxygen and Ethanol electric pumps for rocket engine

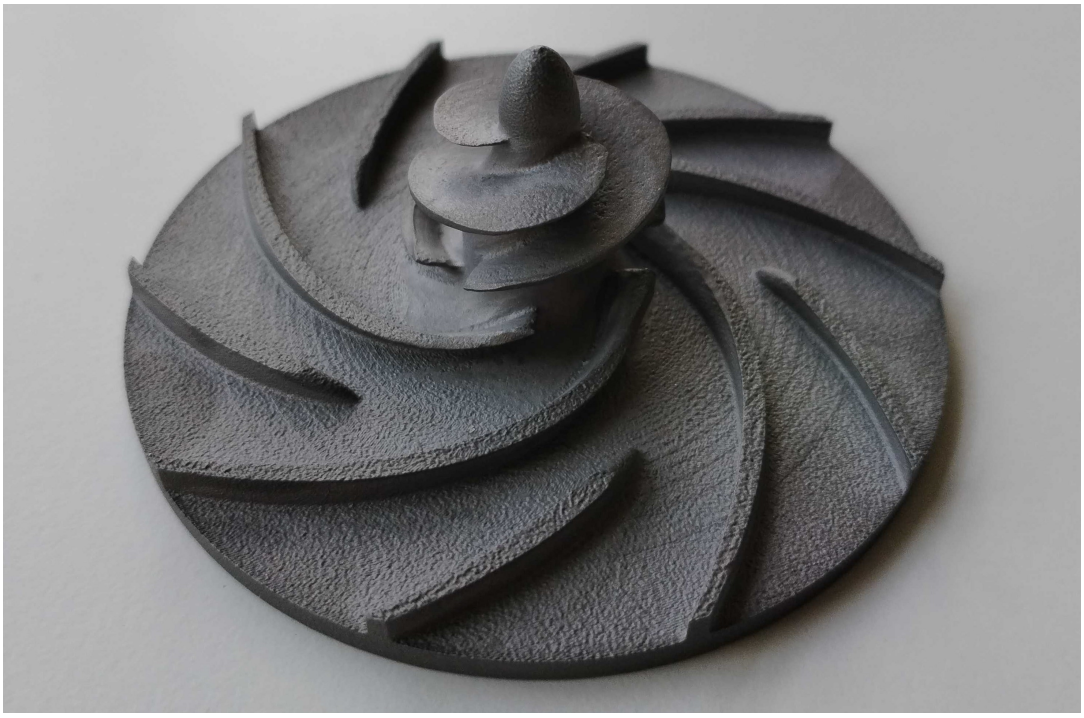

Théotime Lemoine
283379

EPFL

École polytechnique fédérale de Lausanne

Spring 2022

Contents

List of Figures

Acknowledgements

This project aims to size, design and simulate the fluidic section of the future first generation of electric pumps developed by the Hyperion project at EPFL Rocket Team. The future goal is to build and test the first version of these pumps as of next semester and then iterate on the lessons learned from all the prototypes and studies.

As this project is fully integrated into the Hyperion team, I would like to thank the Systems Engineer, Leonard Bongiovanni for his supervision and guidance on the project. Furthermore, I would also like to thank my colleague, Hugo Trombert, for working on the shaft and joint design of the pumps, enabling the team to have a complete design by the end of the semester.

Furthermore, I would like to thank Professor Noca for his supervision and his academic support on this project. Finally, I would also like to thank the CFturbo team for providing their licensed software making this project possible and providing support when necessary enabling us to generate a comprehensive impeller geometry fitting our needs. As well as the Exploration Company Team, working on electric pumps themself and thus providing us precious feed-backs and lessons learned applicable to our design.

Symbols and abbreviations

BC	Boundary Condition
CAD	Computer Assisted Design
CC	Combustion Chamber
CFD	Computational Fluid Dynamics
CNC	Computer Numerical Control
COTS	Commercial of the shelf
ERT	EPFL Rocket Team
GAMG	Geometric-Algebraic MultiGrid solver
LE	Leading edge
LOX	Liquid Oxygen
MRF	Multiple Reference Frame
OP	Operating Point
RANS	Reynolds-Averaged Navier–Stokes equations
SF	Safety Factor
SST	Shear-Stress Transport
TE	Trailing edge

1 Introduction

Hyperion Project

The EPFL Rocket Team (ERT) is a student association whose objectives are to develop and build rockets as well as to explore the different subjects related to such endeavours. At present, the principal objective is to reach space by crossing the Karman line within the next five to seven years using bi-liquids rocket engines.

In order to reach such a goal, a plan with the different technologies to be developed and mastered has been set up for which pump-fed bi-liquid propulsion, cryogenic propellant, and regenerative cooling technologies have been considered crucial to pursue. A long-term goal research project, Hyperion, has thus been set up.

Hyperion project was founded in the summer of 2021 and has since been focused on developing the first generation of bi-liquid engines with several iterations of pressure-fed engines with a peak thrust of up to 1.7 kN. In parallel, a second team has been working on the research aspect and is now working on the development of the second generation of engines, more powerful with a nominal thrust of 5 kN. This second generation, called B-Class engines, aims to incorporate and qualify the technologies presented above (regenerative cooling as well as electric pumps) to increase engine efficiency and extend the flight envelope of our rockets.

The next major step for these B-Class engines is to implement these solutions on several prototypes and perform extensive testing of all the features individually. In a second phase, each of these technologies will be progressively integrated into the rocket engine and iteratively improved thus fully demonstrating the validity of the approach chosen. In the more distant future, these engines and prototypes will pave the way for future classes of engines and enable the EPFL Rocket Team's goal to reach space.

Demo B2 & Electric Pumps

The electric pumps developed in this semester project will be integrated into the future demo-B2 rocket engine which consumes Ethanol and LOX at the flow rates of $\dot{m}_{eth} = 0.71[kg/s]$ and $\dot{m}_{LOX} = 1.14[kg/s]$ to generate 5 kN of thrust. This engine should also be throttleable and integrated with the pumps in a rocket in the future. Thus, in order to provide a mass advantage against a pressure-fed system, the pressure in the tanks should be at a maximum of 6 [bars] resulting in an inlet pressure of 5 [bars] in both pumps. This will be a parameter to account for during the cavitation evaluation in the pumps as we want to avoid this phenomenon to maximize performance.

Table 1. summarize the main pump characteristics and a complete set of requirements can be found in Appendix A.

Table 1: Targeted pumps characteristics

Characteristics		
Propellant	Liquid Oxygen	90 % purity Ethanol
Density	1152 [kg/mˆ3]	785 [kg/mˆ3]
Nominal Flow rate	1.133 [L/s]	1.038 [L/s]
Expected Lifetime	100 s. [± 20 s.]	
Inlet Pressure	5 bar	
Outlet Pressure	38 bar	
Maximum RPM available	40'000 RPM *(Motor choice)*	
Maximum Power available	40 kW *(Motor choice)*	

2 Operating Point definition

The preliminary design for the operating point in turbo-machinery is achieved by relying on similarity concepts using two dimensionless parameters presented in the Barber-Nichols charts.

At this stage of the design process, each pump should be described by its volumetric flow rate (Q), its rotational speed (n), its main diameter (D) as well as its head (H) which can be expressed as,

$$H = \frac{p_{tot,Inlet} - p_{tot,Outlet}}{\rho g} \tag{1}$$

$$Q = \frac{\dot{m}}{\rho} \tag{2}$$

Following the process describes in [2] allows us to relate all these parameters with the targeted efficiency of the hydraulic machine. It also determines the number of stages as well as the type of pump which is optimum for our quantities. In our case, in order to reduce the system's mass and complexity, a single-stage pump design philosophy has been chosen.

The two dimensionless parameters correlating the pump's parameters are the specific speed (N_s) and specific diameter (D_s) and the overall pump efficiency (η).

$$N_s = \frac{n \cdot Q^{1/2}}{H^{3/4}} \tag{3}$$

$$D_s = \frac{D \cdot H^{1/4}}{Q^{1/2}} \tag{4}$$

The required head and mass and volumetric flow rate are given by the requirements in table 1, leaving the efficiency to be empirically selected at 0,5 and 0,6 for the Ethanol and LOX pump respectively.

Thus, as it can be seen in figure 1, the specific speed (N_s) and diameter (D_s) can therefore be selected by reading the chart. As we want to ensure a minimum efficiency for the pumps, the lowest specific speed and highest specific diameter point were selected (red line & red region).

Figure 1: Barber-Nichols Chart with our Region of Interest

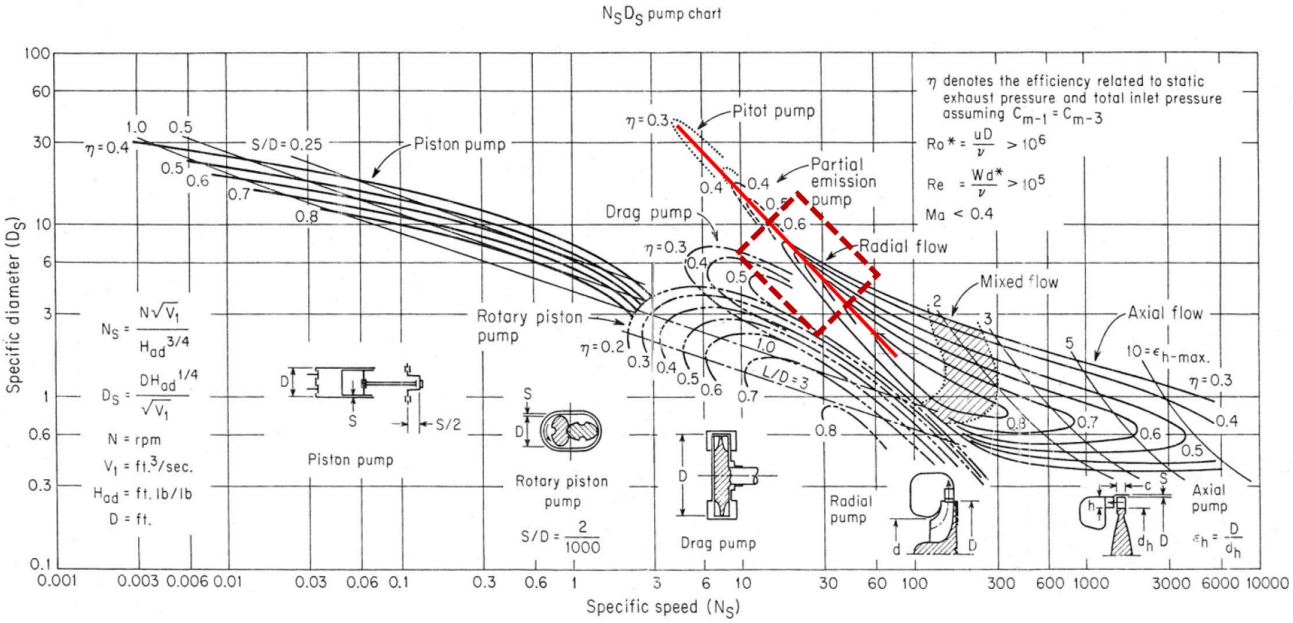

Table 2: Pumps Operating Point characteristics

Characteristics	**Ethanol**	**LOX**
Efficiency η	0.5	0.6
Specific Speed N_s	8.207	12.310
Specific Diameter D_s	8.075 [mm]	6.057 [mm]
Volumetric flow rate Q	1.133 [L/s]	1.038 [L/s]
Rotational Speed H	23'974 [rpm]	25'836 [rpm]
Diameter D	57.2 [mm]	49.3 [mm]
Hydraulic Head H	428.52 [m]	292.01 [m]

Several iterations of this process with respect to the electric motor performance have been computed such that the fluidic design leaves enough margins both in terms of rotational speed and required power for the motor. A potential severe limiting factor is the inception of cavitation, which will be discussed in more detail in the next chapters.

3 Single Stage Euler Theory

As a first approximation to get initial values of the dimensions required for the detailed design of the pump, Euler Theory developed in [3] was used to size the main dimensions of each pump.

For simplicity, these preliminary calculations assume a single-stage radial impeller as defined in section 2 (No inducer has been taken into account, *see section 4*). Moreover, the blockage due to the thickness of the blades, the slip factor and the deviation angle can influence a lot the performance of the pump. Indeed, the thicker the blades, the higher the blockage and the poorest the performance of the pump, including head and efficiency drop. However, these parameters have not been taken into account in these preliminary sizing.

Figure 2: Geometric Nomenclature of the radial Impeller

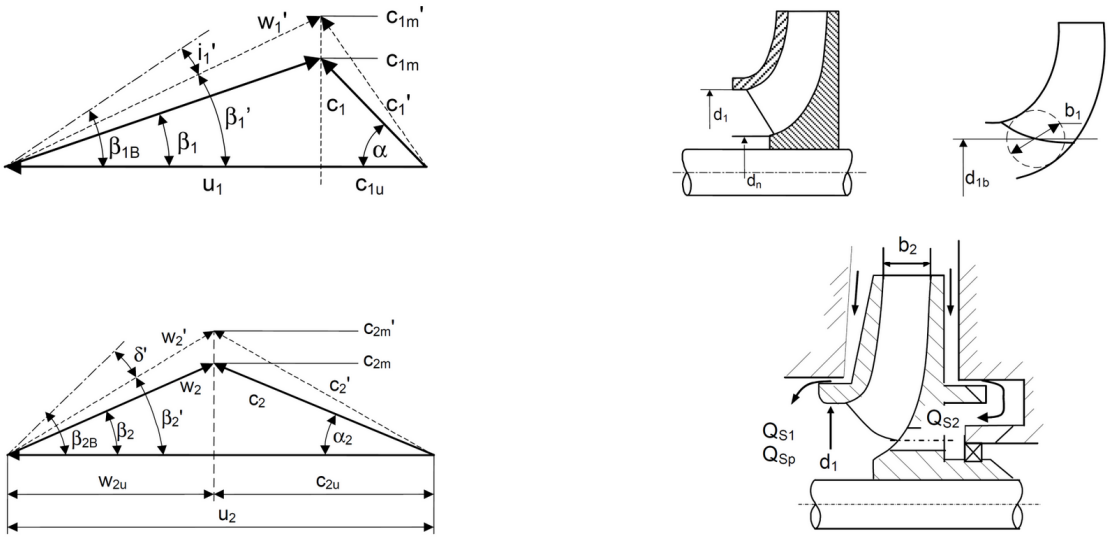

Figure 2 presents the main dimensions of the impeller with the associated velocity triangle.

3.1 Main dimensions

To select the best outer diameter (d_2), one can use the head coefficient $\Psi = 1.21 \cdot e^{-0.77 N_s/100}$. Thus,

$$d_2 = \frac{84.6}{n}\sqrt{\frac{H}{\Psi}} \tag{5}$$

The impeller inlet diameter (d_1) has been selected using the following equation which aims to minimize the inlet relative velocity for minimum leakage, friction and shock losses.

$$d_1 = d_2 \cdot f_{d1}\sqrt{(\frac{d_{hub}}{d_2})^2 + (1.48\Psi\frac{N_s^{1.33}}{\eta^{0.67}} \cdot 10^{-3})} \tag{6}$$

with the coefficient $f_{d1} = 1.1$ and the Hub diameter estimated at $d_{hub} = 14[mm]$

Finally, the outlet width (b_2) can be computed with the help of the outlet width ratio (b_2^*) written as,

$$\begin{gathered} b_2^* = 0.017 + 0.262 \cdot (N_s/100) - 0.008 \cdot (N_s/100).^2 + 0.0093 \cdot (N_s/100).^3 \\ b_2 = b_2^* \cdot d_2 \end{gathered} \tag{7}$$

Table 3 summarises the values of the main dimensions calculated for both pumps.

Table 3: Main dimensions of the impeller from Euler theory

	Ethanol	**LOX**
Inlet Diameter d_1 [mm]	22.1	21.4
Outer Diameter d_2 [mm]	68.5	53.3
Outer Width b_2 [mm]	2.6	2.8

3.2 Velocity Triangle at impeller inlet

Assuming that the inlet flow arrives with no pre-swirl at the inlet of the impeller sets the flow parallel to the shaft axis and thus $\alpha_1 = 90$. Then the following equations can be used to derive the angles and velocities needed :

$$\begin{aligned} u_1 &= \pi \cdot d_1 \cdot \frac{n}{60} \\ A_1 &= \frac{\pi}{4}(d_1^2 - d_{hub}^2) \\ c_{1m} &= Q/A_1 \\ c_{1u} &= c_{1m}/tan(\alpha_1) = 0 \\ w_1 &= \sqrt{c_{1m}^2 + (u_1 - c_{1u})^2} \\ \beta_1 &= arctan(\frac{c_{1m}}{u_1 - c_{1u}}) \\ \varphi_1 &= \frac{c_{1m}}{u_1} \end{aligned} \tag{8}$$

The values computed are summarised in table 4.

Table 4: Velocity vectors at the inlet of the impeller from Euler theory

	Ethanol	**LOX**
Circumferential speed u_1 [m/s]	27.70	29.00
Inlet passage area A_1 [mm^2]	228.6	207.1
Meridional component c_{1m} [m/s]	4.54	5.47
Relative velocity w_1 [m/s]	28.07	29.52
Relative flow angle β_1 [deg]	9.32	10.68
Flow coefficient φ_1 [-]	0.164	0.189

3.3 Velocity Triangle at impeller outlet

The impeller considered is radial such that the outlet is tangent to the plane perpendicular to the shaft axis. This enables us to make several simplifications in the Euler theory resulting in the following set of equations to compute the angles and velocities needed :

$$\begin{aligned}
u_2 &= \pi \cdot d_2 \cdot \frac{n}{60} \\
A_2 &= \pi \cdot d_2 \cdot b_2 \\
c_{2m} &= Q/A_2 \\
c_{2u} &= c_{2m}/tan(\alpha_2) = 0 \\
c_2 &= \sqrt{c_{2m}^2 + c_{2u}^2} \\
w_{2u} &= u_2 - c_{2u} \\
w_2 &= \sqrt{c_{2m}^2 + w_{2u}^2} \\
\alpha_2 &= arctan(c_{2m}/c_{2u}) \\
\beta_2 &= arctan(c_{2m}/w_2) \\
\varphi_2 &= \frac{c_{2m}}{u_2}
\end{aligned} \tag{9}$$

The values computed are summarised in table 5. The negative relative flow angle results for the ethanol pumps come from the low specific speed chosen and will result in complex optimum geometry *(Very large outlet blade angle ($\beta_{B2} >> 90$).*

Table 5: Velocity vectors at the outlet of the impeller from Euler theory

	Ethanol	**LOX**
Circumferential speed u_2 [m/s]	86.03	72.15
Outlet passage area A_2 [mmˆ2]	567.5	439.3
Meridional component c_{2m} [m/s]	1.83	2.58
Circumferential component c_{2u} [m/s]	97.72	66.17
Absolute velocity c_2 [m/s]	97.74	66.22
Relative velocity w_2 [m/s]	11.83	6.52
Absolute flow angle α_2 [deg]	1.07	2.23
Relative flow angle β_2 [deg]	-8.91	23.32
Flow coefficient φ_2 [-]	0.021	0.036

3.4 Volute Design

Finally, the theory developed in the book can also be extended in order to size the volute component of our pump. The volute converts the fluid kinetic energy into static pressure and the goal is to limit as much as possible the potential losses. For simplicity and mass reduction, we will use a single volute with a constant velocity design for the circular cross-section. This design should still be optimum with regard to potential performance losses.

The design can be evaluated using a factor (X_{sp}) to compute the throat area cross-section of the volute (d_{3q} and A_{3q}).

$$\begin{aligned} X_{sp} &= \frac{Q}{\pi \cdot c_{2u} \cdot d_2/2} \cdot \frac{1}{2\pi} \\ d_{3q} &= X_{sp} + \sqrt{2d_z \cdot X_{sp}} \\ A_{3q} &= \frac{\pi}{4} d_{3q}^2 \\ c_{3q} &= Q/A_{3q} \end{aligned} \tag{10}$$

The ratio of throat diameter to impeller diameter in order to prevent pressure pulsation of the discharge pressure can be written as,

$$d_z = (1.03 + 0.1\frac{N_s}{40} + 0.07\rho\frac{H}{1000 * 1000}) \tag{11}$$

As imposed by the requirements in table A, the outlet of the pump should be a 1/2" diameter pipe ($d_{pipe} = 12.7[mm]$), thus :

$$\begin{aligned} A_{pipe} &= \frac{\pi}{4} d_{pipe}^2 = 126.7[mm^2] \\ c_{pipe} &= Q/A_{pipe} \\ Ptot_{pipe} &= p_{out} + \frac{\rho}{2}(c_2^2 - c_{pipe}^2) \end{aligned} \tag{12}$$

The values computed are summarised in table 6. The total pressure computed is lower than the objective of 38 bars as it takes into account some of the losses in the design while having the impeller dimensions based on the ideal pressure difference to reach.

Table 6: Design parameters for a single constant velocity Volute

	Ethanol	**LOX**
Throat Diameter d_{3q} [mm]	5.83	8.43
Throat Passage area A_{3q} [mmˆ2]	26.6	55.8
Volute velocity c_{3q} [m/s]	38.97	20.29
Minimum diameter ratio d_z [-]	0.074	0.084
Pipe outlet velocity c_{pipe} [m/s]	8.20	8.94
Total outlet pressure $Ptot_{pipe}$ [bar]	37.23	37.33

4 Cavitation consideration

4.1 Cavitation Theory

Cavitation is a fluid phenomenon that occurs when the pressure in the flow drops below a critical value called vapour pressure. Driven by the pressure decrease, the fluid changes phase from liquid to gaseous at a specific area of the flow called the cavitation inception area. Thus, when cavitation occurs, a vapour-filled void or cavity forms, causing the streamlines to deviate resulting in a loss of performance due to the uneven loading of the blades. These cavities also have dynamic behaviour which leads to vibrations and mechanical stress on the blades and casing as well as strong erosion when they collapse that will destroy the blades over time.

Figure 3: Various possible types of cavitation in turbo-machinery

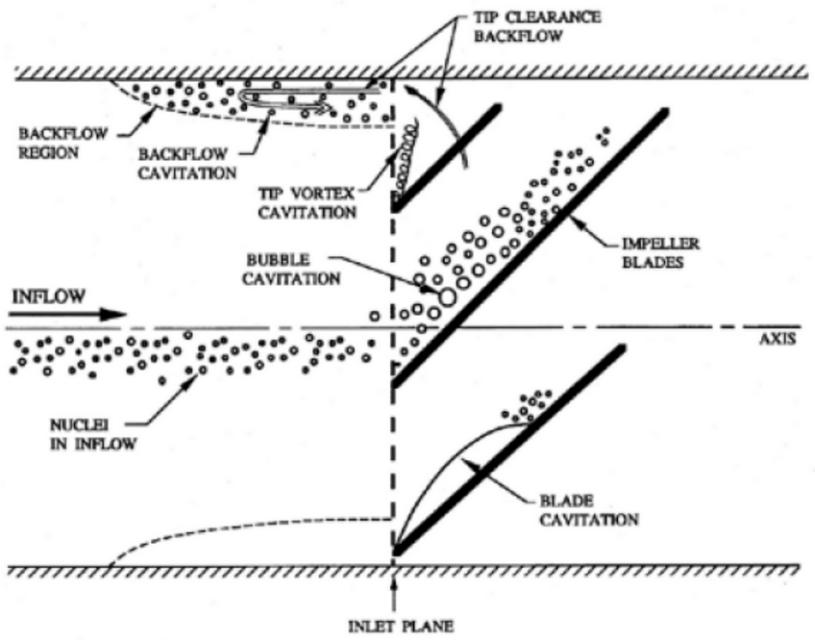

In our case, several types of cavitation can appear as shown in figure 3 *(From [4])* :

- **Inflow Cavitation Nuclei**, which are small vapour bubbles, within the flow will act as formation points for expanding cavities when the pressure drops while the flow is accelerated.
- **Tip Vortex Cavitation** occurs when the flow creates a swirling vortex at the tip of the blade: Such vortex is usually caused by the leakage flow around the blade creating the swirling motion. As the pressure drops in the vortex, cavitation may occur.
- **Back Flow Cavitation** appears near the blade trailing edge when a re-circulation motion appears, decreasing pressure in the area. Thus, cavitation may occur.
- **Blade Cavitation** is created on the suction side of the blade in the proximity of the leading edge and acts as an extra blockage, in addition to the one caused by the blade thickness, thus increasing the hydrodynamic losses.

4.2 Cavitation Prediction

Before fully designing the pump, it is key to try to predict if cavitation may appear. While it is a really complex phenomenon for which theory does not fully represents real flow behaviour, cavitation occurrences can be estimated for our preliminary design. With sufficient margins taken into account, this approach enables us to get a better grasp if cavitation is a serious problem and which solution can be introduced in the pump design.

4.2.1 Leading Edge Cavitation

For the Leading Edge cavitation prediction, one can use the simplistic approach using a corrected Bernoulli relation. Although not very precise, it is simple and we can compute the theoretical pressure drop at the leading edge of the blades. The leading edge pressure p_{L-E} can be computed as

$$p_{L-E} = p_{Inlet} - \frac{1}{2}\rho \cdot \lambda \cdot w_1^2 \tag{13}$$

with lambda (λ) a parameter depending on the blade. This parameter is difficult to estimate before doing CFD or experiments, but the following empirical correlation can be used:

$$\lambda = 3(tan\beta_1)^{0.9} \tag{14}$$

This method aims at predicting cavitation inception on the leading edge of the blades, and not at predicting the development of the cavitation nor the cavity length. The pump should be designed in a way such that static pressure at the LE should be always above the saturation pressure (pv) of the fluids. Results are presented in table 8.

4.2.2 Suction Pressure evaluation

In order to characterise the risk of cavitation in a given pump, the industry practice is to use the Net Positive Suction Pressure ($NPSP$). It is defined as the difference between the inlet static pressure and the fluid vapour pressure. In our case, the pressure rises in the pump can be expressed as the height of the fluid column, the Net Positive Suction Head ($NPSH$).

$$NPSP = p_{Inlet} - pv \quad NPSH = \frac{NPSP}{\rho g} \tag{15}$$

These quantities are however dimensional and thus specific to our pump. Using the cavitation number (σ) allows to judge the similarity of flows with cavitation. It relates the $NPSP$ to the dynamic pressure based on blade tip speed at the inlet :

$$\sigma = \frac{NPSP}{\frac{1}{2}\rho w_1^2} \tag{16}$$

In order to avoid cavitation with sufficient margins, the cavitation number should be much higher than 1. Table 8 presents the results of these calculations, where it can be seen that cavitation might be a concern for the LOX pump with a cavitation number of only 1.121.

Table 7: Cavitation prediction estimation for our pumps

	Ethanol	**LOX**
Vapour pressure pv [Pa]	4'020	10'340
Leading Edge pressure p_{L-E} [Pa]	347'753	216'061
Margins [-]	86.5	20.9
$NPSP$ [Pa]	495'980	489'660
$NPSH$ [m]	65.46	43.33
Cavitation number σ [-]	1.603	1.121

4.3 Cavitation Prevention

Several techniques and design strategies can prevent cavitation such as the tweaking of the blade angles or a particular attention to the surface roughness of both the impeller and the casing. In addition, other features such as grooves in the casing to straighten the flow, and special rounded shapes of the blade leading edge to reduce the size of the low-pressure zone. However, in this section, two other design philosophies will be presented: adding an inducer stage and adding splitter blades onto the impeller. Both features, while not totally necessary in our case, have been implemented in order to experiment with them and thus allowing us to have more freedom in our future pump designs.

4.3.1 Inducer

Inducers are widely used in the field of high-speed turbo-machinery and especially with rocket engine pumps. The philosophy is to add a first axial impeller at the inlet to raise the fluid static pressure before the main radial impeller. Typically, the inducer has a specific shape, as shown in figure 4, featuring a sharp leading edge and thinner blades, and is designed to operate with very little incidence relative to the flow to minimize cavitation. Indeed, at a very low incidence angle, cavitation will form only on the suction side of the blade and therefore preserves the pressure side, the most critical one. With a typical energy fraction from 1 to 10 %, an inducer will potentially increase the impeller inlet total pressure by up to 3 bars.

Figure 4: Inducer under cavitating conditions *(From [1])*

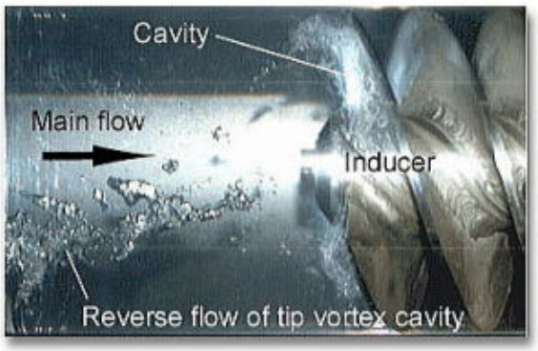

One can finally note, that using an inducer extends the operating range of the pump therefore allowing an increase in rotational speed thus leading to a reduction of dimensions and mass.

4.3.2 Splitter blades

A splitter blade is a blade whose length has been reduced such that its leading edge is shifted downstream as seen in figure 5.

Figure 5: Radial impeller featuring two types of splitter blades

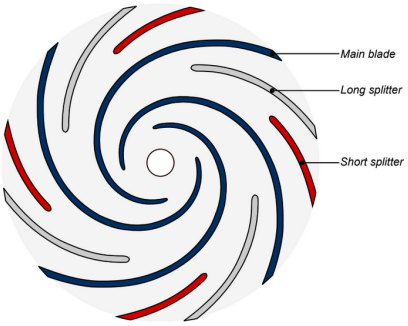

Such configuration brings two major benefits with respect to cavitation :

- By shifting the blades outwards, their leading edge is in a higher total pressure zone, thus the potential for leading edge cavitation for these blades is significantly minimized.
- The other immediate effect is to reduce the blade blockage by having fewer blades at the inlet. Reduced blockage translates into lower velocities, hence higher pressures and reduced cavitation development compared to a traditional impeller. Less or shorter blades imply higher loads and so slightly reduce performance. However, splitter blades reduce the flow deviation at the outlet, offsetting this loss of efficiency.

Overall, the literature review ([5], [6]) confirms the benefit of adding splitter blades with regards to cavitation issues as well as improving the pump efficiency and performance due to the flow being better aligned with the blade at the impeller outlet.

5 Design of the Pumps

The final design for the impeller of both pumps has been done using a COTS software, CFturbo, whose offered license and support made this project possible. It is based on the same theory as the calculations done previously but provides several empirical corrections, correlations, and more complex models. Furthermore, the software generates CAD models used as a starting point for the CAD design and the simulation workflow.

Both pumps will be designed as semi-open (unshrouded), to ease as much as possible the manufacturing after consultation with workshops. Moreover, both pumps will feature an inducer and splitter blades to add extra margins with respect to cavitation as well as to minimize performance losses *(see section 4)*. Indeed the prediction computed does not take into consideration a lot of parameters that might influence cavitation inception such as blade thickness or the LE shape. Finally, soft stainless steel is considered to be the material of choice for both pumps with a total allowable stress of 115 [MPa] *(see section 6)*.

5.1 Ethanol Pump Design process

Design targeting the operating point defined in 2 is done with the ethanol properties detailed in Appendix B. Multiple iterations of this process with feedback have been done to generate a satisfactory design of the ethanol pump.

Using the multi-stage feature, both the inducer *(as a special type of axial impeller)* and the radial impeller are created. The total pressure rise from the inducer (Δp_{ind}) is set to 3.5% with the left achieved by the impeller. This results in a pressure rise of 1.16 [bar] with the associated specific speed of $N_{s,ind} = 101$. Finally the tip clearance s_{Tip} has been set to 0.15 mm ($\frac{s_{Tip}}{d_2} \in [0.015; 0.04]$).

First, the impeller is designed with the shaft diameter $d_{hub} = 14[mm]$ set to resist all the loads with a minimum safety factor of 3. Automatic values for the inlet & outlet diameter (d_1&d_2) as well as outlet width (b_2) are used. The outlet diameter had then to be slightly enlarged to $d_2 = 76[mm]$ in order to ensure correct flow angle *(Euler theory has some corrective factor at low specific speeds)*. Shock-less entry is used to design the inlet angle of the impeller $\beta_1(r)$ and an outlet angle $\beta_2(r) = 19.3$ is chosen to limit the outlet flow deviation to 20° for best efficiency. The number of blades chosen is $Z_{imp} = 5$, and a set of 5 splitter blades are added at 50% of the diameter. Then, the blade shape is manually tuned to be flat enough to avoid re-circulation and stall to the maximum extent while preserving sufficient overlapping at around 3.5 (wrap angle set to 126°). The LE is chosen rounded to reduce cavitation and the maximum blade thickness is set to 2 [mm] to ensure sufficient margins with regards to stress. Similarly, the impeller base has a thickness set at 3 [mm], well above the 0.87 [mm] computed by the program *(Adding the SF of 3)*. Secondary flow paths are then generated with 0.2 [mm] thickness at the tip and TE of the blade. In order to avoid the suction effect and better equalize the pressure at the back of the impeller, the secondary flow path thickness s_{back} is set to 2 [mm].

The next component designed is the inducer. It is designed to have an outlet that matches the impeller inlet (both d_1 and $_{hub}$). At the inlet, the inducer diameter is computed to be $d_{1,ind} = 22.9[mm]$ and the hub diameter is set to $d_{hub,ind} = 6.9[mm]$. The number of blades (Z_{ind}) is set to 3 with a shock-less entry and automatic flow angles using the free vortex model. The blade shape is then tuned to reduce the camber and limit the tip losses. The LE and TE are chosen rounded to reduce cavitation and the maximum blade thickness is set to 1.2 [mm] to ensure sufficient margins with regards to stress. Adding an inducer modified the flow angles for the impeller that thus have to be updated with a similar procedure.

The volute is designed with a circular cross-section with a quadratic area expansion to maximize volumetric efficiency. The design follows the constant velocity rules from Stepanoff. The cut-water diameter is automatically computed, $d_{cut} = 7.0[mm]$ well above the minimum computed in equation 11. $d_{cut,min} = 5.62[mm]$. The outlet of the pump had a 1/2" diameter as required in Appendix A to integrate with the plumbing of the engine. Thus a diffuser has to be created, with a cone angle of 4.2° to minimize losses and footprint (Length = 50 [mm]) .

Finally, additional features are added to the pump to finalize the design :

- As the inlet is required to have a 1/2" diameter *(see Appendix A)*, a diffuser is created upward of the inducer to match its inlet diameter $d_{1,ind}$. With a length of 32.5[mm] and smooth transitions to minimize both losses and size.
- A cone with a matching slope for a smooth transition is designed to sit on top of the inducer hub to minimise shock losses. The cone has a height of 6 [mm].
- An axial stator has been added between the inducer and the impeller to allow the generation of secondary flow paths. This stator potentially reduces flow interactions between the blades and eases manufacturing.
- An radial stator has been added between the impeller and the volute to allow the generation of secondary flow paths. This also increases the TE clearance for the impeller thus reducing the pressure pulsation risks.

All the key values of the ethanol pump design are detailed in the CFturbo reports in Appendix C. As the chosen specific speed is low and below 10, one can comment that Euler's theory and CFturbo design models need to be validated and potentially tuned both with CFD simulations and physical testing. Figure 6 shows the different stages and features of the ethanol pump in its final designed iteration.

Figure 6: Meridional view of the ethanol pump using CFturbo software

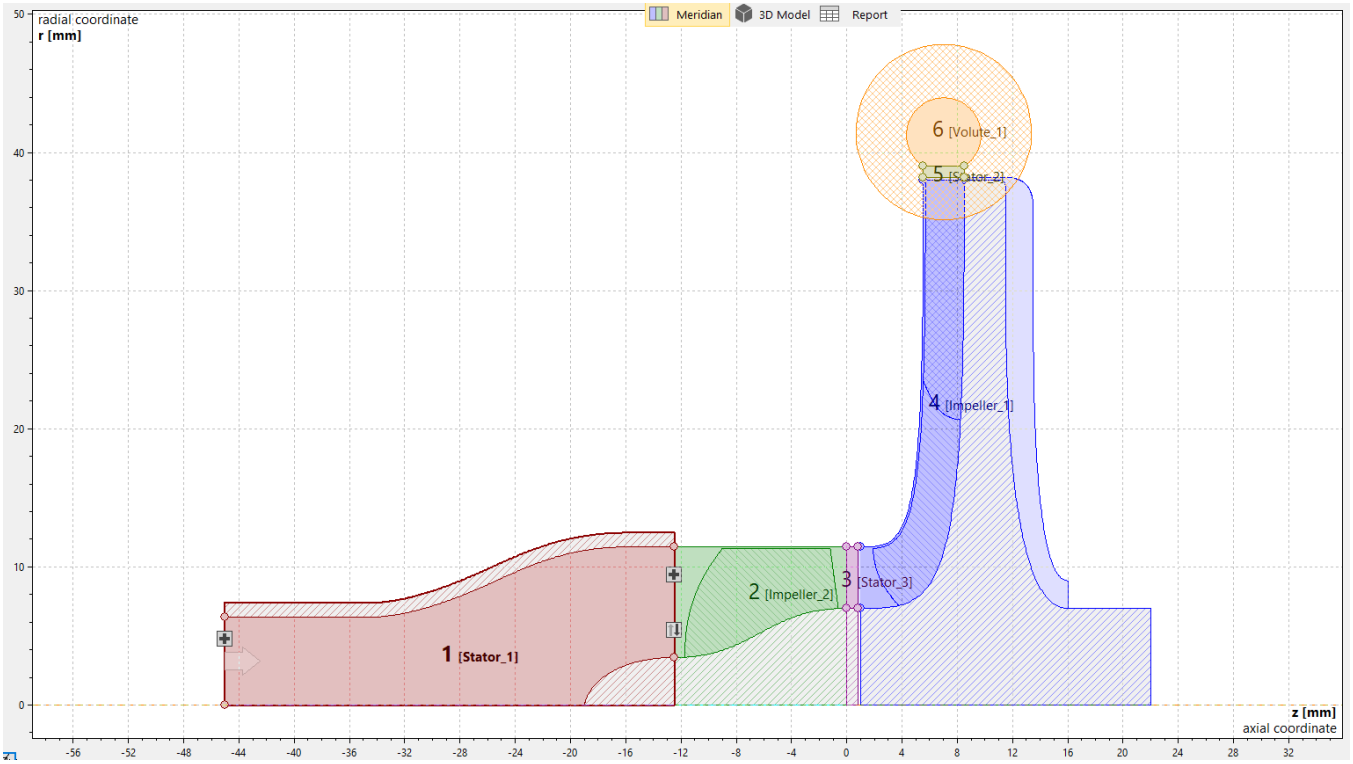

5.2 LOX Pump Design process

The LOX pump design follows a very similar process as explained in detail in subsection 5.1 and only key changes will be mentioned here with the set of values used in CFturbo to be found in Appendix C.

- The total pressure rise from the inducer is (Δp_{ind}) raised to 6% , resulting in a similar specific speed of $N_{s,ind} = 101$.
- Due to the important thermal constraints at cryogenic operating temperature, the tip clearance of the blade is extended to 0.2 [mm] *(Same for the secondary path thickness).*
- The shaft diameter is kept constant, $d_{hub} = 14[mm]$, to ease manufacturing of other pieces.
- The inducer diameter is $d_{1,ind} = 22.5[mm]$ with hub diameter set to $d_{hub,ind} = 6.75[mm]$.
- The outer diameter have been enlarged to $d_2 = 55[mm]$ while the outlet flow deviation is maintained to 20°, with thus an outlet angle $\beta_2(r) = 21.1$.
- There is 4 main with 4 splitter blades with an overlapping of 2.45 (wrap angle set to 110°).
- Maximum blade thickness is adjusted to 0.8 [mm] for the inducer and 2 [mm] for the impeller.
- The cut-water diameter is $d_{cut} = 7.6[mm]$ well above $d_{cut,min} = 4.6[mm]$.
- The diffuser is adjusted with a length of 46 mm and a 3.9° cone angle.

While having a specific speed above 10, performances and potential fine-tuning would also have to be performed after CFD simulations and physical testing. Figure 7 shows the different stages and features of the LOX pump in its final designed iteration.

Figure 7: Meridional view of the LOX pump using CFturbo software

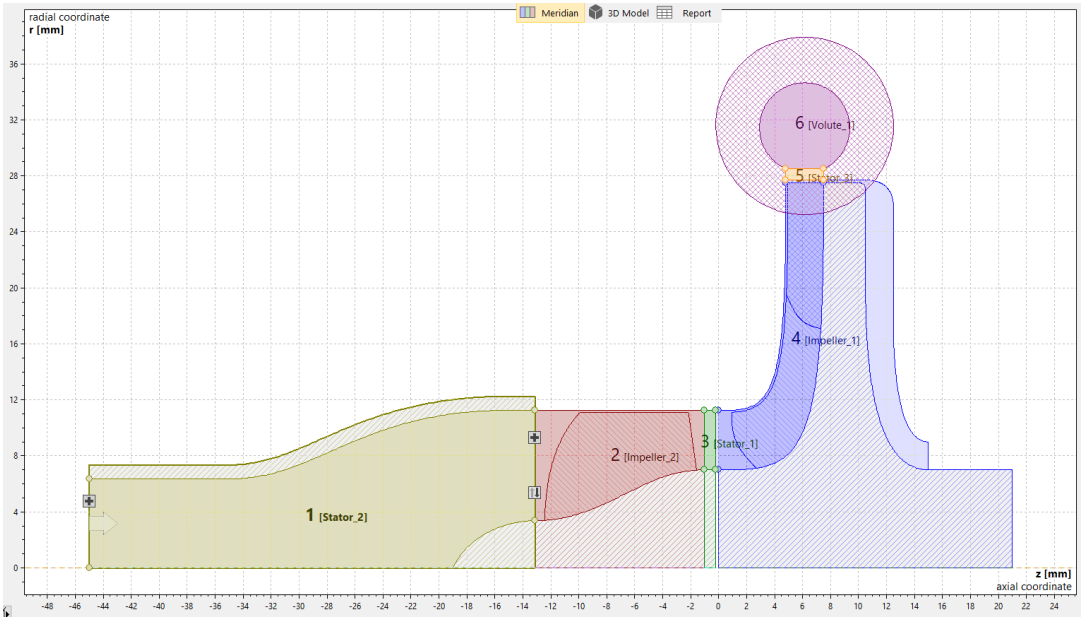

5.3 Design Results & Estimated Performances

CFturbo allows us to predict the results of the designed pumps by providing an estimation of the various losses seen by the pump. However, while the cavitation is not taken into account in this analysis, the presence of an inducer and splitter blades should result in a relatively good prediction. Figure 8 generated by CFturbo presents ideal performance based on Euler's theory *(upper black line)*, the various computed losses *(coloured regions)* and the final characteristics *(lower red curve)* in Δp-Q graph called Euler wet performance diagram. One can note that by enlarging the impeller diameter d_2, additional margins with regards to our original rotational speed operating point are expected *(distance between the red curve and black circle)*.

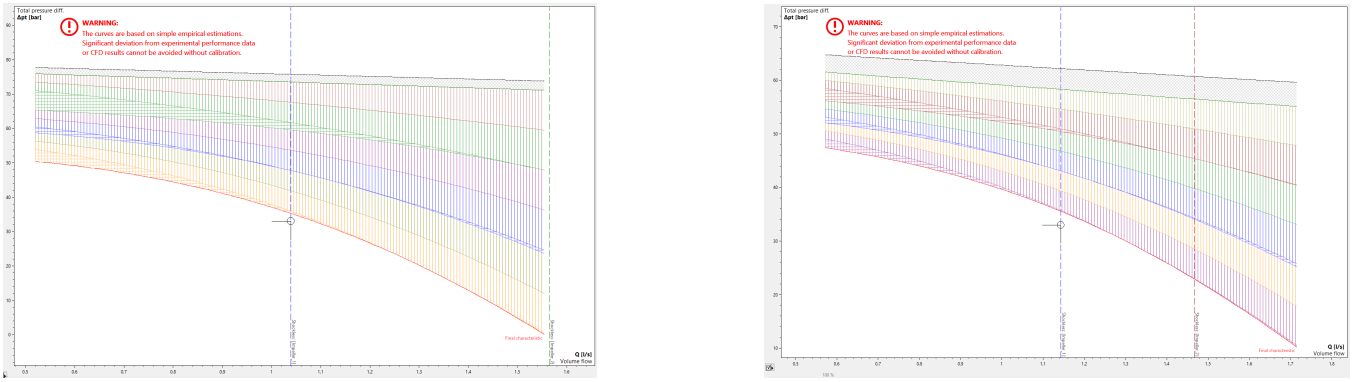

(a) Ethanol Pump (b) LOX Pump

Figure 8: Δp-Q curve predicted by CFturbo

6 Casing design and Manufacturing

As the next upcoming steps for the pump project at EPFL Rocket Team are to manufacture, assemble and test the pump to characterise its practical behaviour and performance, special care has been given to the design of the impeller and its casing in this project. The design generated by CFturbo has thus been adapted with feedback from the EPFL workshop in order to make it easier & cheaper to manufacture. The exact same modifications, as presented in this section for the ethanol pump, are made for the LOX pump as can be seen in Appendix D.

6.1 Impeller Modification

Several modifications have been done to the impeller itself in order to use 5 Axis CNC to machine it. This manufacturing process ensures very high precision with strict tolerances as well as a low roughness on the surface. Surface roughness is critical for cavitation inception and CNC machining guarantees a surface finish of at least $R_a < 1.6[\mu m]$. Other processes such as casting and moulding have been deemed too expensive and not precise enough for our case. Also, metal 3D printing seems to be a valid approach but will need a lot of post-processing to ensure a good precision and surface finish. A prototype has been manufactured *(see figure 9.)* with this technique assessing its validity but emphasises the large post-processing works needed when compared with CNC machining that can be done in the workshop of EPFL and thus the chosen manufacturing technique for the impellers.

Figure 9: 3D Printed Impeller manufactured

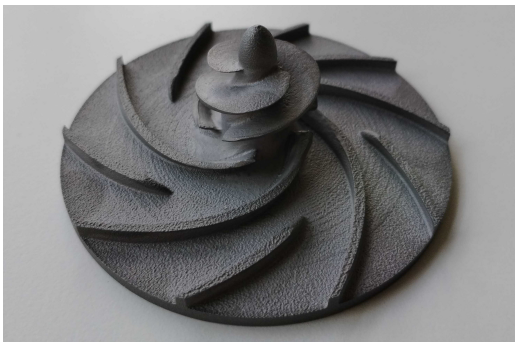

The following is a list of all the modifications made :

- Rounding of the blade base ($R = 0.6[mm]$) to allows for larger tools to be used.
- Rounding and enlarging at the back & hub of the impeller to strengthen the design.
- 6 [mm] cylindrical extension at the back of the impeller featuring flats for assembly.
- Inner tapping with a centring bore to interface the impeller with the pump shaft.

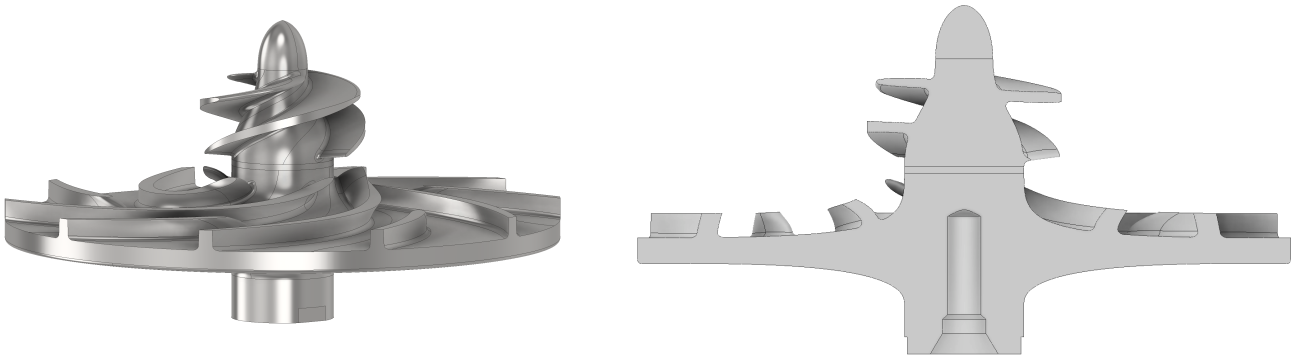

(a) 3D View (b) Cutaway View

Figure 10: Ethanol Pump Impeller final design

6.2 Casing Design

The casing has been designed in two parts split in the middle of the volute such that it can be easily assembled and disassembled. Such separation also greatly eases the tool path as these parts will also be CNC machined. In order to fully seals the casing a static PTFE joint (Sourced from Maagtechnic[1]) is added and will be compressed when the casing is closed. 6 M6 screws ensure closure and clamping between the two parts.

[1]https://shop.maagtechnic.ch/fr/joints-d-etancheite-joints-toriques-o-rings-et-accessoires-joint-torique-o-rings/joint-torique-ptfe-pr-ec010583-0001/ [Accessed 18/05/2023]

At the Inlet and Outlet, "1/2–14 G" threading are tapped to integrate the pump with the engine's plumbing. A centring bore is added at the back of the casing with a PTFE joint (Sourced from Maagtechnic) and 6 M4 screws tapping to assemble the casing with the rest of the pump.

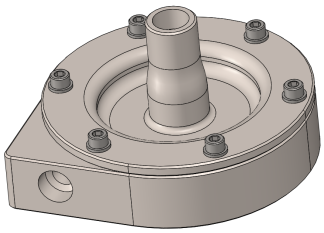

(a) 3D View

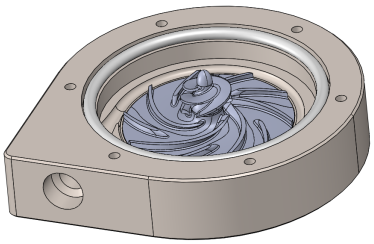

(b) 3D View opened

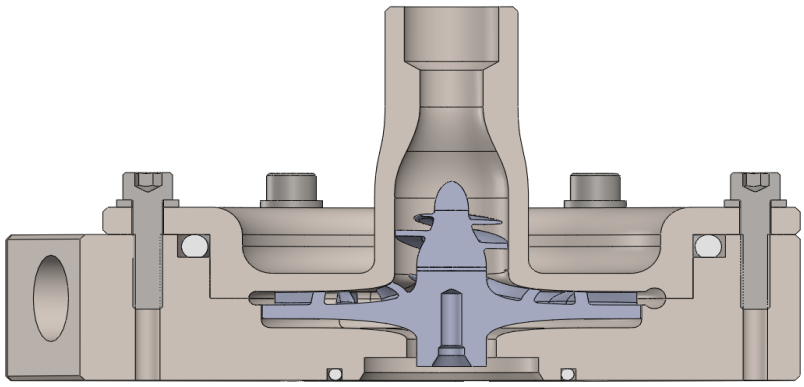

(c) Cutaway View

Figure 11: Ethanol Pump casing assembly

The upper part of the casing, as shown in figure 27, is only 3 [mm] in order to potentially monitor cavitation with microphones mounted on top. However, microphones might not be precise enough to isolate cavitation from all the other sources of noise. Thus, another casing using transparent materials to have direct oversight of the region of interest for cavitation inception *(Mainly the inducer)* might be needed. In any case, an additional iteration of this design will need to be performed in the loop with the rest of the pump assembly and the EPFL workshop feedback.

7 Fluidic Simulations

Numerical CFD simulations were performed in order to evaluate more precisely the performances of the pump designed in section 5. Complex geometries and thus potentially complex fluid dynamics coupled with the inherent approximations used in such simulations make them an important first step within the scope of this project, but cannot entirely substitute the physical testing required to fully characterize both pumps.

7.1 Numerical Simulation Workflow

An initial workflow has been put in place with the philosophy of maximizing the use of open-source software accessible to the general public. The free and widespread availability of such solutions supported by a large community makes them really attractive and to some extent customizable to the project's need while ensuring the long-term viability of the approach. Moreover, as one of the goals of this semester project is to learn valuable skills, knowing how to use open-source software is a really valuable skill set as there are widespread across the industry.

In this workflow, the fluid domain geometry is generated by CFturbo *(COTS)*, with the meshing performed with SALOME *(open Source)* and the CFD simulation and post-processing done using Open-FOAM & para-View *(open Source)*.

Although preliminary simulations (simplified mesh, 360° complete geometry, steady state) were carried out using the described workflow *(see Appendix E.)*, the refinement of the mesh, in particular the generation of a matching inflation layer, lead to various errors that did not allow these detailed simulations to be carried out. Particularly, the Netgen algorithm used to generate the mesh created a small number of invalid cells (high skewness, negative volume, under-determined cells ...) that lead to the error in running the math of the open-FOAM code. Despite many attempts, and even with a really detailed & periodic mesh, these mesh errors were still present that prevented detailed simulations to be performed. Finally, using a mesh generated using ANSYS and featuring no critical errors for OpenFOAM math was not possible due to the limited CPU capabilities of the computer used.

Since the inflation layer is key to properly simulating the flow, especially with respect to the turbulence model used, it has been decided to modify the workflow integrating COTS solutions. As ERT is fortunate to have them as sponsors, CFturbo was directly integrated with the ANSYS framework with the mesh being generated using ANSYS Meshing tools and the simulation performed by CFX.

7.2 Numerical Simulation Set-up

7.2.1 Key assumptions

Table 8: Key assumptions for the CFD simulations conducted

The flow is in steady conditions
The flow is incompressible
The effects of gravity are negligible
The fluid is single phase (No cavitation)
The flow is isothermal (Heat transfer negligible)
Fluid-structure dynamical interactions are negligible
Geometrical deformation linked to the rotation of the impeller is negligible
The leakage rate by the joints is set to 1% of the total outlet mass flow rate

7.2.2 Geometry & Boundary Conditions

This section presents the considered domain and the associated Boundary Conditions (BC) for both pumps as well as the setup used to carry out these simulations. As both pumps have a really similar design, the work done is nearly identical, thus only the Ethanol Pump will be illustrated for this part *(see Appendix D for the final LOX Pump mesh)*.

In order to save computational time and memory, the fluid domain has been reduced taking advantage of the periodicity properties of the blades. The final domain used in the simulation, as presented in Figure 12, features 5 different subdomains detailed as :

- **Inlet** including the 1/2" inlet extension, a diffuser until the inlet section of the inducer with the cone. This subdomain is axis-symmetric and thus only a third of it is considered.
- **Inducer** including the inducer stage of the pump. This subdomain is axis-symmetric and thus only a third of it, centred around the blade mean surface, is considered.
- **Axial stator** including only the axial stator. As a rather small subdomain, the full 360 geometry is considered
- **Impeller** including the impeller stage of the pump. This subdomain is axis-symmetric and thus the geometry centred around one of the main blades' mean surfaces is considered *(A fifth in the case of Ethanol and a fourth in the LOX case)*.
- **Volute** include the volute and the associated stator. No axis-symmetry exists in these subdomains meaning the full 360 geometry is considered.

Figure 12: Periodic fluid geometry domain used

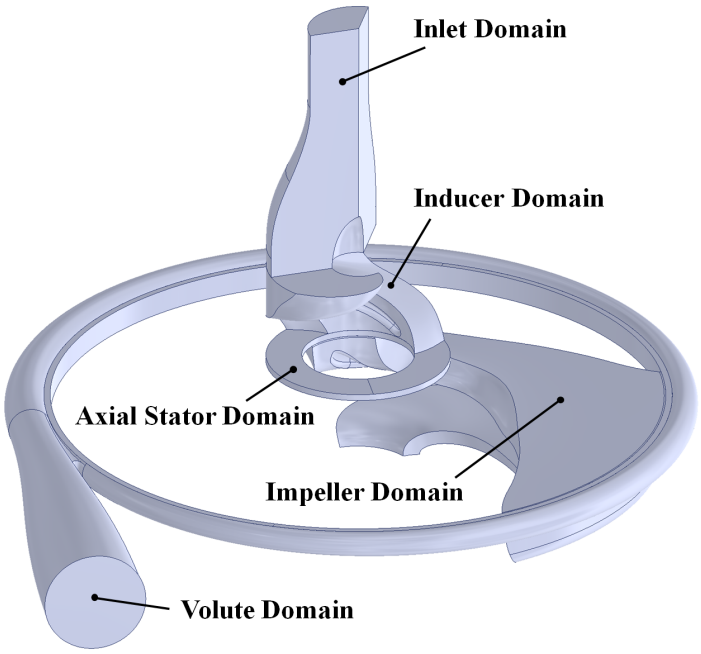

In order to handle the rotation of the pump, all subdomains were created to have a rotational motion with the exception of the Volute which is stationary. Thus, the mesh in these regions will rotate with the fluid while the exterior wall and shroud of the casing will have to be set stationary (counter-rotating the mesh).

Associated with these domains comes numerous different BC to determine how the flow and the geometry will behave at the edges of the studied domain. Figure 13 details the application area of each BC detailed in the following list :

- **Total Pressure Inlet** The Total pressure at the Inlet of the pump is set to 5 [bars] according to the requirements (*see Appendix A*).
- **Fixed Mass Flow Rate Outlet** Both the outlet of the pump and the secondary flow path outlet have a fixed mass flow rate boundary condition: With 0.816 [kg/s] at the main outlet and 0.00816 [kg/s] to fulfil the performance requirements and take into account the worst case leakage (*see Appendix A*).
- **Static Rough Wall** All the impeller walls have a static wall with no slip in the rotational frame. The roughness is set to 1.6 [microns], corresponding to the worst surface roughness possible using CNC machining. Similarly, the Volute domain walls feature the same boundary condition in the stationary frame.
- **Counter rotating Rough Wall** To handle the pump rotation properly, all the shroud walls of the rotating domains *(Inlet, Inducer, Axial Stator & Impeller)* are set to be a counter-rotating and no-slip wall in the rotational frame. The roughness is also set to 1.6 [microns] for the same reasons.
- **Rotational Periodicity** A rotational periodic boundary condition has been set to the patches handling the axial symmetry of the considered reduced fluid domain.
- **Frozen Rotor Interfaces** All the interface between each subdomain is handled using a General Grid Interface with conservation of all flux. The frozen rotor option has been selected in order to map all the variables directly to the neighbour patch.

7.2.3 Turbulence & Numerical methods

Both pumps are simulated using the RANS model SST $k-\omega$, which is the most widely used turbulence model for internal flows, especially in turbo-machinery. This model is preferred over $k-\epsilon$, as the latter has difficulties with accurately modelling adverse pressure gradients and flow separation. Although the $k-\omega$ turbulence model does not need any wall function, one should be careful with the y+ value in order to resolve accurately the boundary layer. Indeed common practices consider regions with a $y+$ value below 1 accurate, and sufficiently accurate for value below 5. This requires in our case a very refined mesh along all the walls which, coupled with the complex blade geometries, leads to a very heavy mesh.

However, in ANSYS, the automatic wall function can be used in the least interesting or less critical regions enabling the wall yPlus to be in a much wider range from 30 to 300. For more accurate results, the meshes have been created (see section 7.3) with a target of 30 or 50 for the wall yPlus, saving computational memory and time.

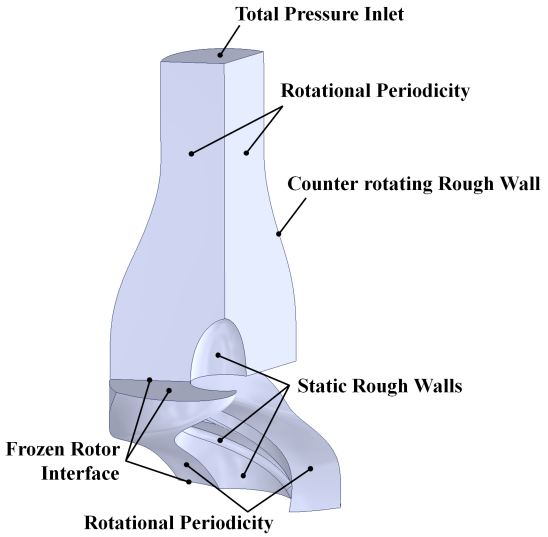

(a) Around Inlet & Inducer domains

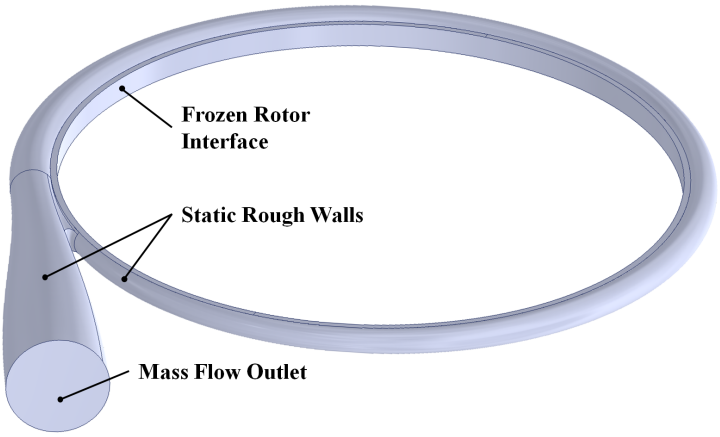

(b) Around Volute domain

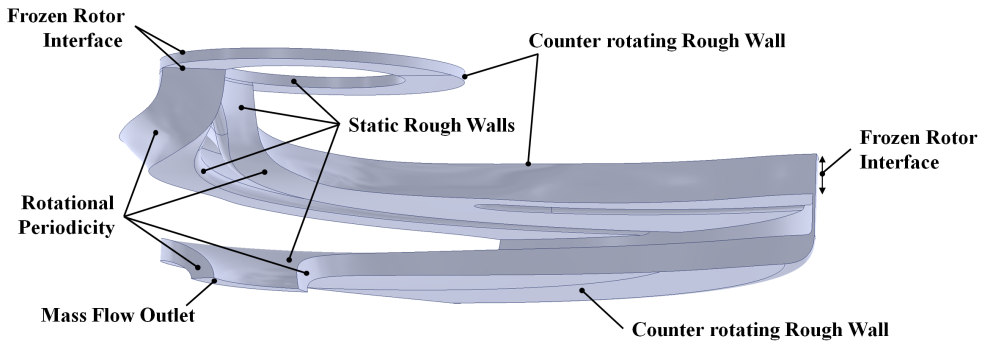

(c) Around Axial Stator & Impeller domains

Figure 13: Boundary Conditions applied to the fluid domain

The CFD simulations have been carried out using the CFX program from ANSYS, which is superior for rotating turbo-machinery with respect to Fluent and is particularly effective for flows with strong swirling, re-circulation and highly three-dimensional characteristics. Thus, a high-resolution advection scheme coupled with a high-resolution turbulence numerics solver has been used to take full advantage of the above-mentioned benefits.

Standard initialization has been used, by setting up no initial velocity and a constant static pressure field of 5 [bars] in the rotational frame. Timescale and length scaling are automatically adjusted by the CFX solver with the conservative option to ensure stability and efficient convergence. As the flow behaviour can be quite complex, manual adjusting of the timescale factor has been done to improve numerical stability.

7.3 Meshes

7.3.1 Pump Domain Meshing

To generate the full mesh, each domain described previously is meshed independently and then connected together using a General Grid Interface boundary condition. All the domains have been meshed using the ANSYS Mesher with the CFX generation parameter set-up, creating mainly tetrahedral elements with the exception of the Inducer domain, which has been meshed using TurboGrid, enabling to create a high-quality mesh mainly featuring Hexahedra elements despite the complex geometry. The Impeller domain didn't use such a preferred method due to geometrical constraints and the presence of a secondary flow path (It is aimed to implement a TurboGrid meshing in the future). Peculiar attention was given to the refining of the near-wall meshes, crucial for the resolution of the boundary layer. Due to the low kinematic viscosity of liquid oxygen, the direct resolution of the boundary layer was scarcely possible for reasonable mesh size and solving time. Thus the use of wall functions was required for the LOX Pump, with a targeted yPlus between 30 to 80 instead of yPlus ≤ 5 usually needed. The Ethanol Pump was meshed with sufficiently refined inflation layers to be directly resolved without wall functions.

Figure 14 to 18 presents the various details and domains of the final mesh generated for the Ethanol Pump and similar figures for the LOX Pump can be found in Appendix D.

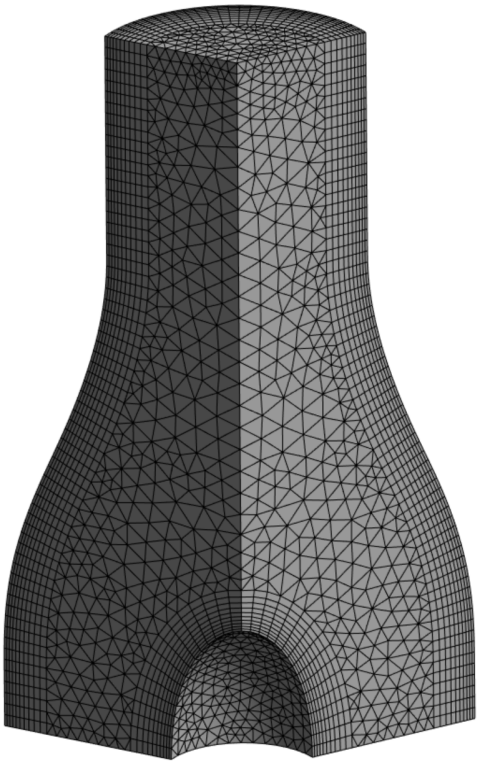

(a) 3D View of the Inlet extension mesh

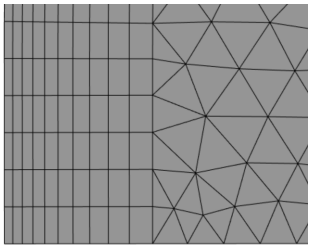

(b) Inflation Layer detail

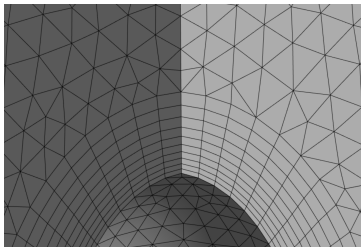

(c) Top of Cone detail

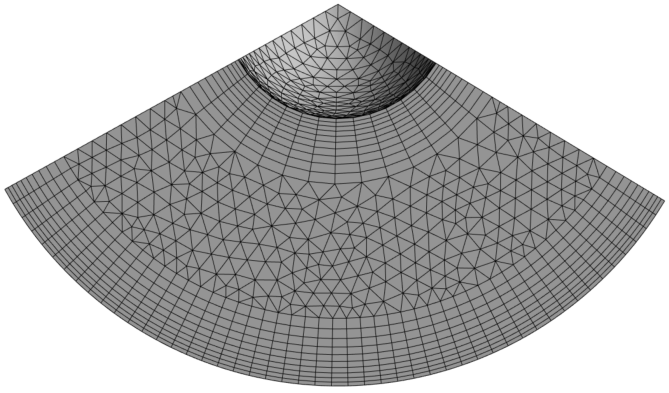

(d) Back of the Inlet extension View

Figure 14: Generated Mesh for the Inlet extension domain of the Ethanol Pump

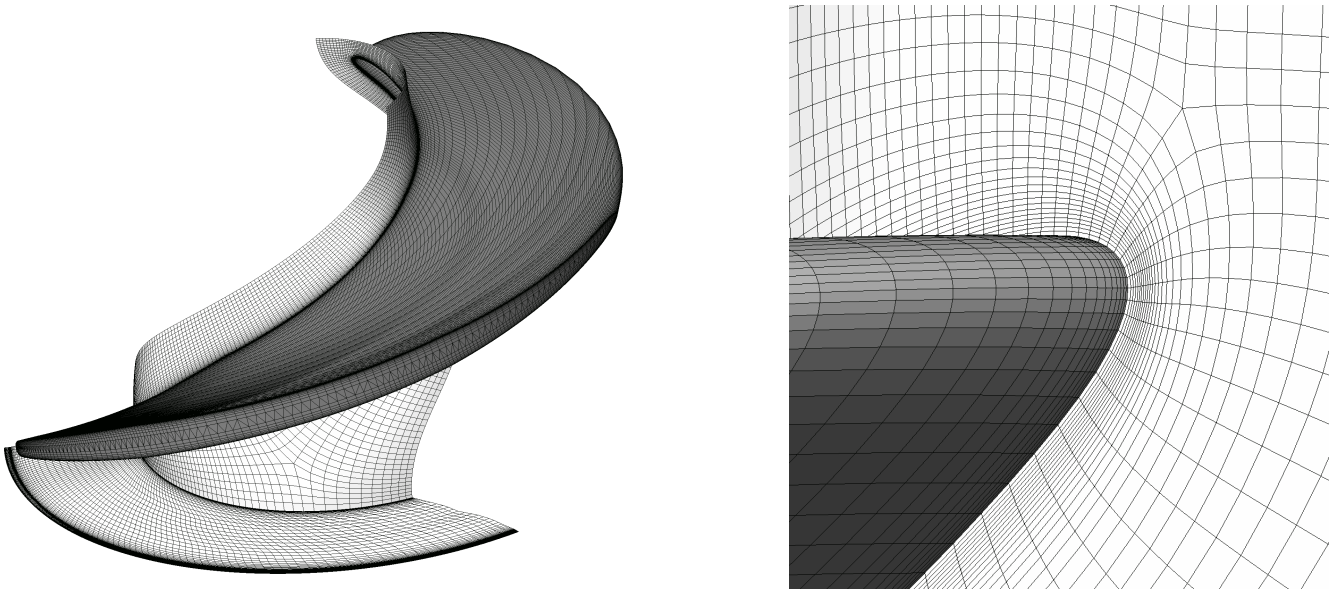

(a) 3D View

(b) Leading Edge Hub detail

Figure 15: Generated Mesh for the Inducer of the Ethanol Pump

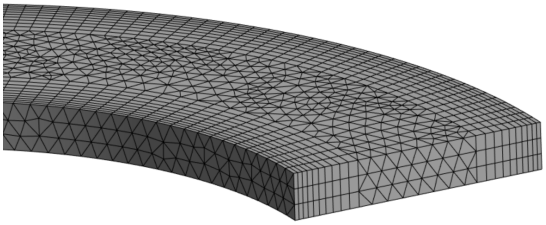

Figure 16: Generated Mesh for the Axial Stator domain of the Ethanol Pump

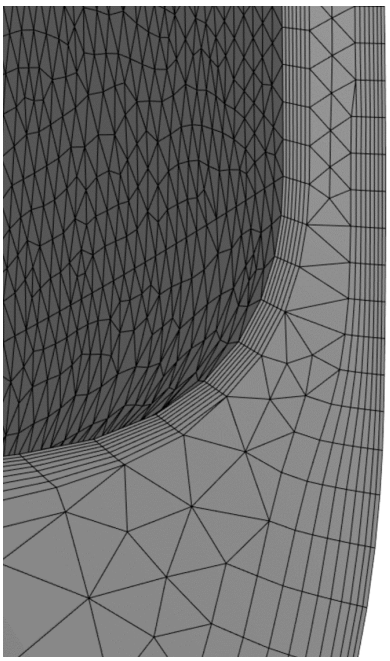

(a) Inflation Layer detail

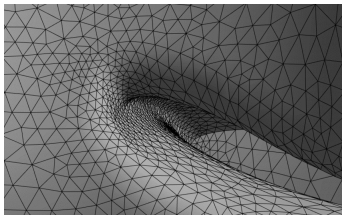

(b) Main Blade LE detail

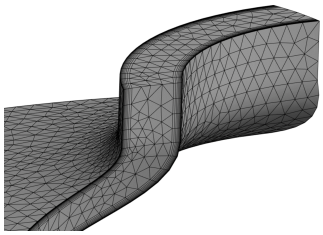

(c) Leakage Outlet detail

(d) 3D View

Figure 17: Generated Mesh for the Impeller domain of the Ethanol Pump

(a) 3D View

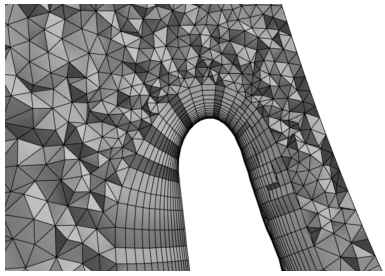

(b) Cut-water Cutaway detail

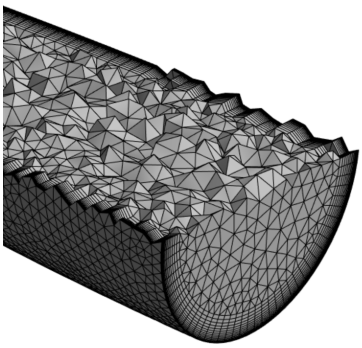

(c) Outlet Cutaway detail

Figure 18: Generated Mesh for the Volute domain of the Ethanol Pump

Mesh quality and heaviness were evaluated using various relevant metrics as presented in both tables 9 and 10. One can note that the overall quality of elements is rather low at around 0.5 in order to limit the computing requirements. This trade-off is mainly penalised by the impeller domain featuring a lot of elements but has a rather poor quality *(Average Element Quality around 0.4 to 0.41)*. New meshing methods taking advantage of the TurboGrid mesher to generate a high-quality mesh should really improve the quality while keeping the heaviness acceptable.

Table 9: Ethanol Pump Mesh Metrics

Heaviness	**Nodes Number**	**Elements Types**	**Elements Number**
Inlet Domain	35'447	Tetrahedra & Prism	88'567
Inducer Domain	497'329	Prism & Hexahedra	473'538
Axial Stator Domain	8'712	Prism & Tetrahedra	20'950
Impeller Domain	673'082	Prism & Tetrahedra	1'659'653
Volute Domain	178'940	Tetrahedra & Prism	519'582
Total	1'393'510		2'762'290
Global Metrics	**Lowest**	**Average**	**Highest**
Orthogonality angle [°]	2.19	74.26	89.80
Edge Length ratio	1.01	15.49	1025.28
Element Volume ratio	1	2.43	123.86
Aspect Ratio	1.09	17.29	516.07
Skewness	$6.85e-6$	0.258	0.985
Average Element Quality		0.504	

Table 10: LOX Pump Mesh Metrics

Heaviness	**Nodes Number**	**Elements Types**	**Elements Number**
Inlet Domain	48'900	Tetrahedra & Prism	115'101
Inducer Domain	986'024	Hexahedra	939'020
Axial Stator Domain	10'441	Tetrahedra & Prism	21'754
Impeller Domain	890'825	Prism & Tetrahedra	2'261'090
Volute Domain	396'412	Tetrahedra & Prism	980'492
Total	2'332'602		4'317'457
Global Metrics	**Lowest**	**Average**	**Highest**
Orthogonality angle [°]	2.48	76.28	89.92
Edge Length ratio	1.03	32.98	1304.20
Element Volume ratio	1	2.22	155.6
Aspect Ratio	1.13	35.64	758.16
Skewness	$4.44e-5$	0.243	0.994
Average Element Quality		0.502	

7.3.2 Convergence Monitoring

The convergence of both simulations is defined using a Root Mean Square criteria (RMS) of 10^{-4} for the normalised residuals of the momentum and continuity equations. To ensure that such a target results in convergence of the flow behaviour several monitor points have been set up to evaluate the average outlet pressure of both the main and leakage outlet as well as the minimum pressure in both the inducer and the impeller. As presented in Figure 19, the convergence is reached after 299 time-steps for the Ethanol simulation and after 728 time-step for the LOX simulation. Such differences between both pumps may be explained by the different fluid properties *(kinematic viscosity and density)* and mesh differences *(mainly the inflation layer and its wall functions)*.

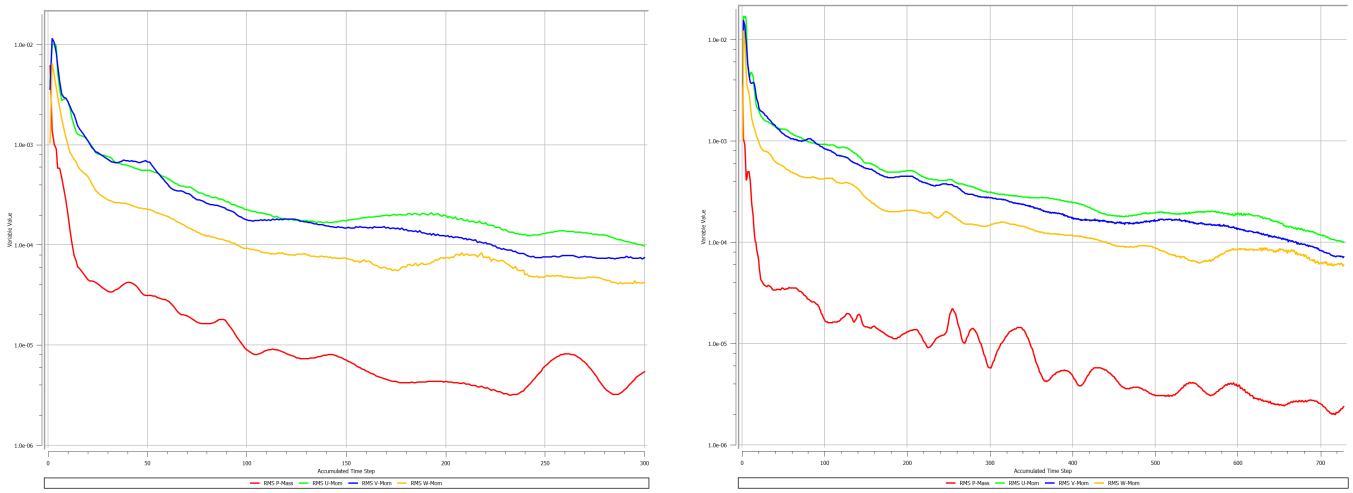

(a) Ethanol Pump Simulation (b) LOX Pump Simulation

Figure 19: Momentum & Mass residuals convergence

7.4 Results

7.4.1 Ethanol Pump Results

Figure 20 shows the velocity streamlines in the rotational frame for all the domains excepted in the volute which is stationary and thus with the streamlines represented in the stationary frame. All streamlines are coloured by the velocity magnitude in the stationary frame.

As seen in the figure, the streamlines show a large recirculation area in the diffuser of the volute with high vorticity. Such behaviour will cause head losses and potential vibrations on the pump. A possible way to improve the outlet flow would be to reduce the expansion ratio of the diffuser, which would mean a smaller adverse pressure gradient with respect to the flow. However, in order to reduce both mass and space, a simple extension of the casing and the diffuser was not considered and a suitable solution will have to be found before integration into a rocket.

Figure 20: Velocity streamlines in the Ethanol Pump

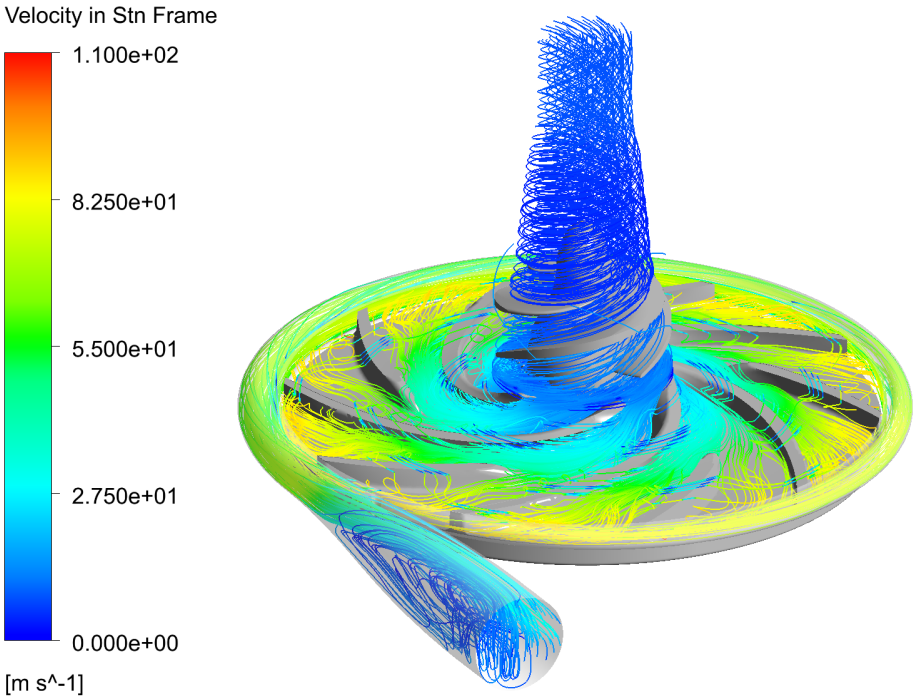

Figure 21 shows the total pressure behaviour across all domains of the pump to better understand the flow distribution and the performance of the pump. One can note that the vast majority of the pressure rise occurs within the impeller, where we can see the highest-pressure zones of all the pumps, just in front of the blades and especially the splitter blades.

Moreover, the total pressure in the diffuser reaches around 55 bars *(54.37 bars at the outlet)*, indicating that the pump seems to vastly over-perform according to these simulations *(targeted total pressure of 38 bars)*. These differences will be addressed later in the final numerical results section 7.4.3. It is also worth noting that the total pressure loss linked to the recirculation in the diffuser seems to be minimal, with an almost imperceptible pressure gradient in Figure 21a. Finally, the leakage outlet at the back of the impeller has a lower total pressure than expected at around 30 bars *(31.43 bars at the leakage outlet)*. The theory expected the back total pressure to be equivalent to the outlet total pressure since the secondary flow path starts between the impeller and the volute, where all the pump energy has been delivered to the fluid.

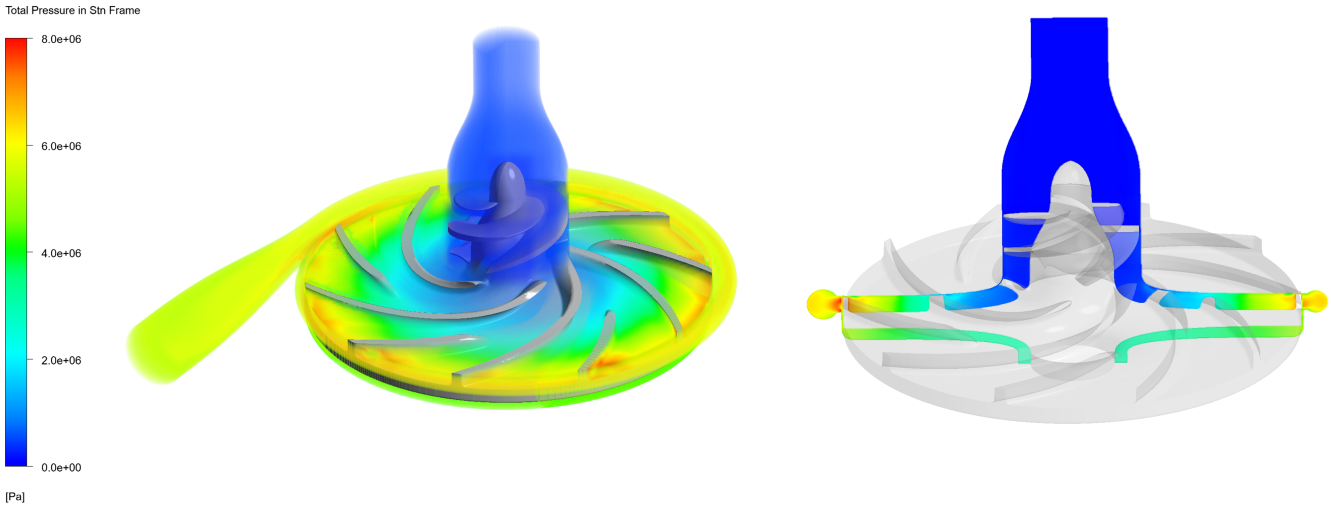

(a) 3D View (b) Cutaway View

Figure 21: Total pressure in the Ethanol Pump

Figure 22 shows the static pressure on the impeller in order to monitor the cavitation inception and help to qualitatively evaluate stress on this part. In order to prevent cavitation, the static pressure shall be at every point superior to the vapour pressure of the fluid. One can check at the LE and the tip of the inducer blades as these are the area where the static pressure is expected to be the lowest. Indeed, as shown in Figure 22b, the tip of LE of these blades sees the lowest static pressure of around 2.47 bars, well above the pressure vapour of ethanol *(around 4'000 [Pa])*, which drastically reduces the risk of cavitation.

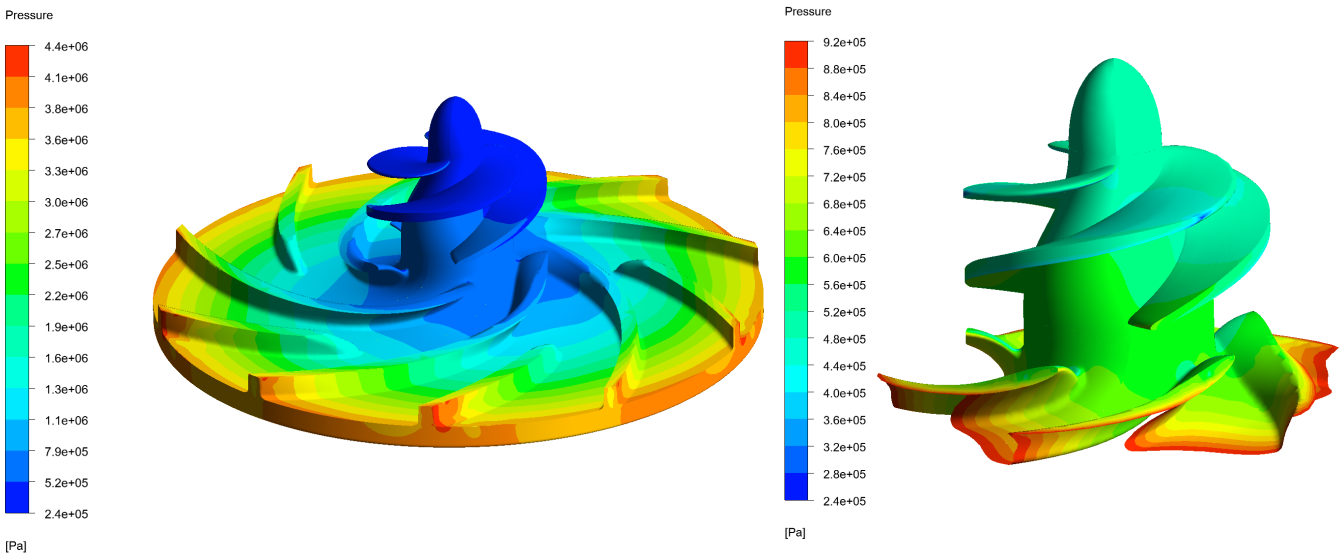

(a) Impeller View (b) Inducer detail

Figure 22: Static pressure on the Ethanol Impeller

7.4.2 LOX Pump Results

Figure 23 shows the velocity streamlines in the rotational frame for all the domains excepted in the volute which is stationary and thus with the streamlines represented in the stationary frame. All streamlines are coloured by the velocity magnitude in the stationary frame.

As seen in the figure, the streamlines suggest a potential small recirculation area in the diffuser of the volute. If such behaviour appears, it will cause head losses and potential vibrations on the pump, thus making it crucial to monitor recirculation and avoid it. A possible way to improve the outlet flow would be to reduce the expansion ratio of the diffuser, which would mean a smaller adverse pressure gradient with respect to the flow. However, in order to reduce both mass and space, a simple extension of the casing and the diffuser was not considered and a suitable solution will have to be found before integration into a rocket.

Figure 23: Velocity streamlines in the LOX Pump

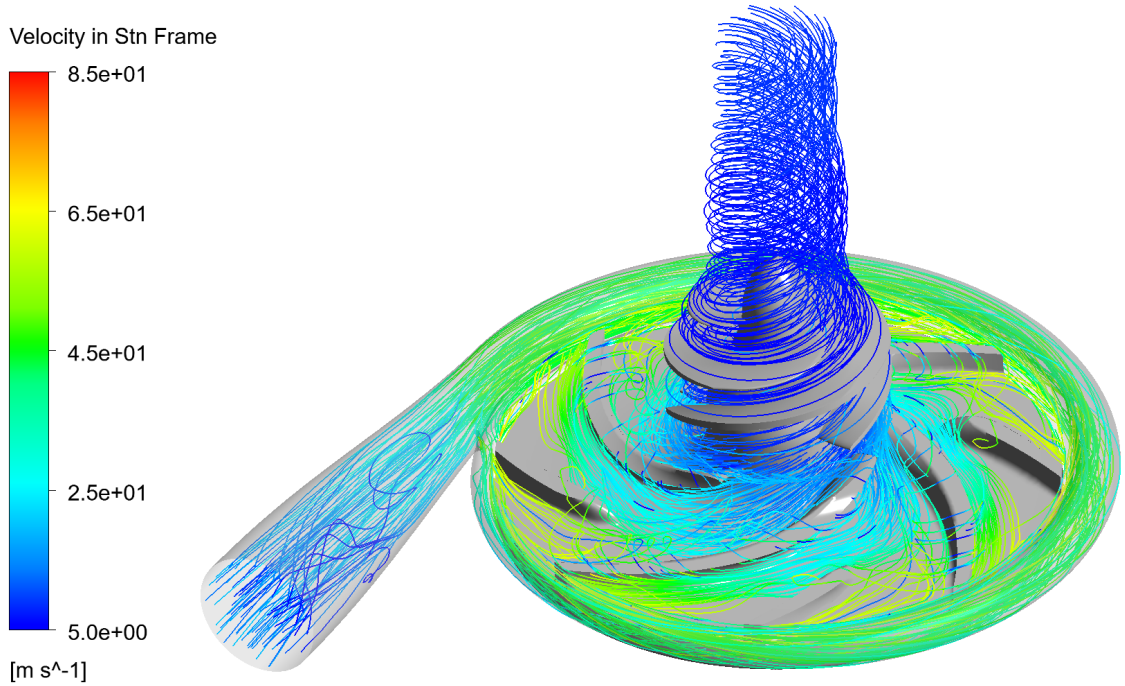

Figure 24 shows the total pressure behaviour across all domains of the pump to better understand the flow distribution and the performance of the pump. One can note that the vast majority of the pressure rise occurs within the impeller, where we can see the highest-pressure zones of all the pumps, just in front of the blades and especially the splitter blades.

Moreover, the total pressure in the diffuser reaches around 45 bars *(42.20 bars at the outlet)*, indicating that the pump seems to over-perform according to these simulations *(targeted total pressure of 38 bars)*. These differences will be addressed later in the final numerical results section 7.4.3. It is also worth noting that the total pressure loss linked to a potential recirculation in the diffuser seems to be minimal, with an almost imperceptible pressure gradient in Figure 24a. Finally, the leakage outlet at the back of the impeller has a lower total pressure than expected at around 25 bars *(26.81 bars at the leakage outlet)*.

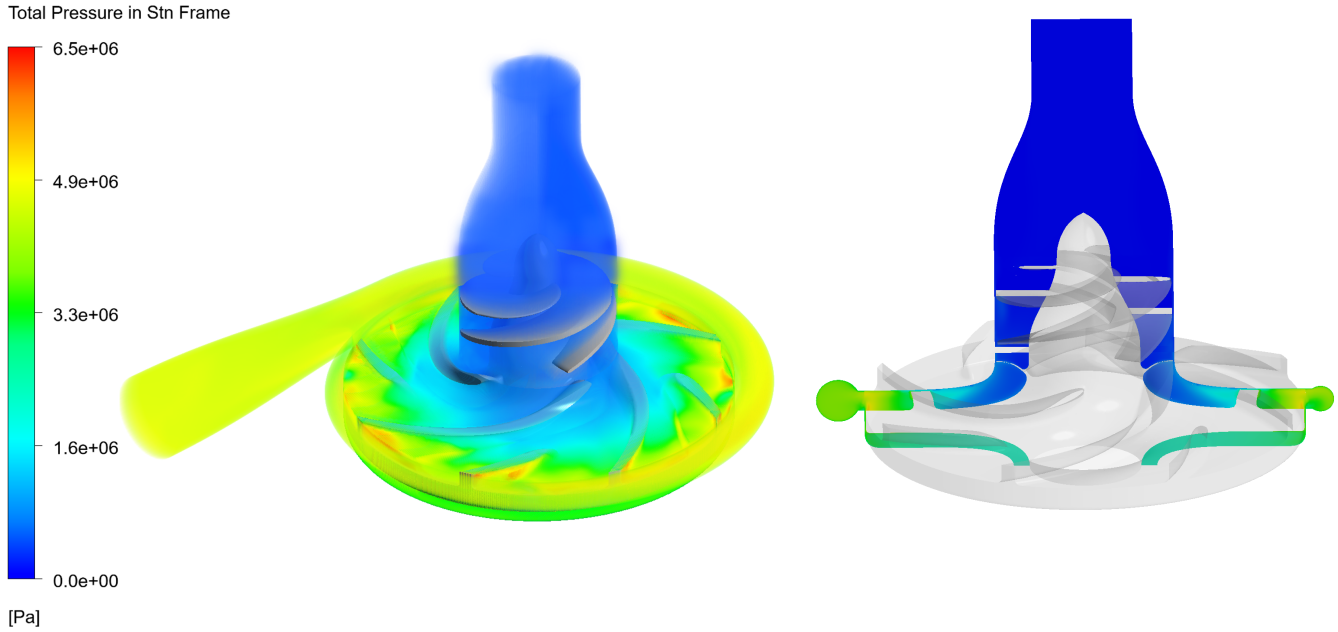

(a) 3D View (b) Cutaway View

Figure 24: Total pressure in the LOX Pump

Figure 25 shows the static pressure on the impeller in order to monitor the cavitation inception and help to qualitatively evaluate stress on this part. One can check static pressure at the LE and the tip of the inducer blades as these are the area where the static pressure is expected to be the lowest. Indeed, as shown in Figure 25b, the tip of the inducer blades sees the lowest static pressure of around 2.25 bars, well above the pressure vapour of ethanol *(around 10'000 [Pa])*, which drastically reduces the risk of cavitation.

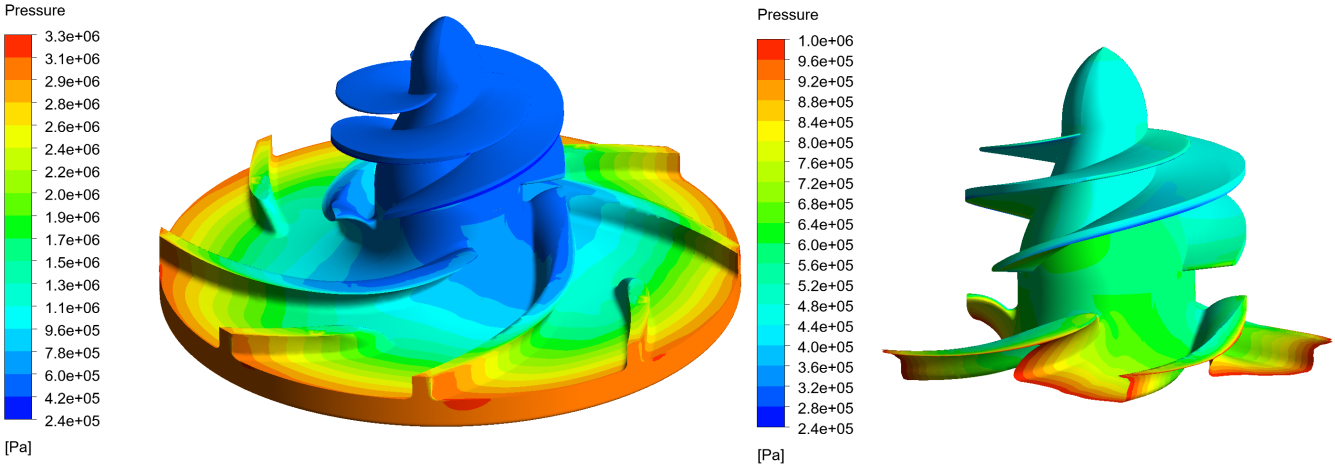

(a) Impeller View (b) Inducer detail

Figure 25: Static pressure on the LOX Impeller

7.4.3 Final Numerical Results

Table 11, presents the numerical results for the key values of both pump performances in the steady state regime considered. One can note that, according to the CFD results, both pumps over-perform in their operational regime with pressure rise superior to the 33 bars required. However, this comes at a cost of a higher torque needed to rotate the pump. This could be a major issue in our design case since the electric motor doesn't have sufficient margins to provide this new torque *(Maximum torque around 4.5 [Nm]).*

This mismatch between simulations and theoretical sizing is therefore one of the priorities to address with the first tests assessing the pump's real performance. Indeed, it can be expected that the CFD simulations will over-predict the performances since some losses are not accounted for in CFD (Volumetric losses for example) as well as the geometry and physical behaviour *(rotation of the impeller)* are idealized. This gap between simulation and real performance is hard to estimate with no prior experience on similar prototypes and design processes, emphasizing the importance to start building and testing these pumps as soon as possible.

Finally, the introduction of an inducer and splitter blade seems to have greatly reduced the risk of cavitation inception in the pump with sufficient margins. It is therefore not necessary to perform additional simulations of the two-phase flow evolution of potential vapour cavities at this stage. However, cavitation should still be monitored in the pump testing and especially in different operating regimes.

Table 11: Performances prediction for our pumps using CFD

	Ethanol	**LOX**
Performances		
Main Outlet Pressure P_{out} [bars]	54.37	42.20
Outlet Margins [%]	143	111
Torque & Forces on the Impeller		
Rotating Torque T_z [Nm]	5.57	3.41
Margins with CFturbo [%]	156	124
Axial Force F_z [N]	5'827	2'383
Leakage		
Joint Outlet Pressure P_{Joint} [bars]	31.43	26.81
Average Velocities V_{Joint} [m/s]	14.90	21.92
Swirl Ω_{Joint} $[s^-1]$	3097.13	3291.17
Cavitation		
Vapour pressure pv [Pa]	4'020	10'340
Inducer LE Pressure $p_{LE,Ind}$ [Pa]	247'703	225'460
Cavitation Number [-]	2.38	2.52
Impeller LE Pressure $p_{LE,Ind}$ [Pa]	463'958	431'100
Cavitation Number [-]	3.24	1.61

8 Final discussion

8.1 Points to be clarified

- During the design of the pump it has been noted that Euler's theory, upon which the sizing is based, introduces, especially at low specific speed N_s, a lot of uncertainties on the blade angles leading to rather extreme shapes. The literature review allowed us to solve the problem by assuming that the slip deviation of the flow at the impeller was around 20°. This however has to be confirmed by CFD analysis and then looped back into the pump's design until convergence is reached. This process has not been done since extra margins have been taken on the pump performances and a large gap with the theory has been observed. Physical testing has to be carried out to assess if refinement in the design is needed to achieve targeted performances.

- The CFD simulation to validate the performance of the pumps relies on many assumptions and neglects the fluid-structure interaction that could see the impeller slightly deformed and thus change its performance. Similarly, the LOX pump has also been considered isothermal with no heat transfer nor thermal deformation of the impeller as the startup procedure has been defined such that the pump is first thermalised and then started. Nevertheless, these simplifications introduce some small uncertainties on the CFD results but above all raise the question of running simulations to assess the thermal properties and deformations as well as the mechanical strength for both impeller *(Thermal, Forces & Modal simulations)* and casing *(Thermla & Forces mainly)*.

- The project considered only the steady state at the nominal operating point. However, the pump must be accelerated to this speed and the engine throttling capabilities lead to time variation of pump rotation speed to adjust the mass flow rate of both propellants. These effects would need a dedicated study on their own to determine the various operational procedures of the pumps, modifications of the design and impacts on performance (cavitation, re-circulation and modal resonances). With this respect, transient simulations to asses the time-dependent flow behaviour when throttling the pump should therefore be carried out and later validate with physical testing.

8.2 Futures considerations

This semester, two projects have been taken to produce on one hand the design of the fluidic part of the pump (impeller & casing) and on the other hand the mechanical assembly of the shaft and joints of the pump. In parallel, work has been done on the electronics as well as the future test bench. Thus, the next steps as of this summer are to iterate on the binding between the two parts of the pump and then start the manufacturing process (high availability of EPFL workshops). The goal is to start the testing campaign on the Ethanol pump (no cryogenics to handle) as soon as next semester to validate the behaviour and performances of the pump. Then, a phase of optimization by iterating on the design will be carried out before integrating it into a rocket in the near future .

In the course of this project, some questions on the direction chosen as well as other research opportunities have emerged if the ERT continues its work in turbo-machinery :

- If ERT continues to develop low specific speed turbo-machinery, it might be interesting to investigate other shapes than centrifugal impellers: As an example, engineers at the Exploration Company suggested considering Barske Impeller, which is suited for such application. Indeed such impeller shapes only have minimal performance deficit with respect to centrifugal impellers while being much simple and cheaper to manufacture.
- On top of Euler's theory, the design process relies heavily on empirical models and correlations, thus it might be interesting to investigate specific models best suited for ERT application cases. One could, for example, implement a data-driven approach mixed with CFD simulations and testing results to design future pumps that would be truly optimized for our use case.
- While this project didn't manage to successfully implement detailed pump simulation using the open source approach, this type of workflow seems very interesting to pursue, given the formative purpose of ERT. However, dedicated work on implementing such a solution coupled with more powerful dedicated hardware *(Cluster of CPU for example)* may unlock the full benefits of this open-source approach. In this case, a dedicated semester project with the goal of better simulating the pump (adding fluid-structure interactions and time dependencies of the impeller rotation) could be beneficial to ERT.

8.3 Conclusion

To conclude this project, the objective to characterize and reach a comprehensive design of the fluidic part of ERT future electric pumps have been achieved, starting with a simplified theoretical approach based on Euler's theory. Then, several iterations of incorporating a more complete model using CFturbo software, while taking into account manufacturing and assembly constraints, enabled me to obtain a final, detailed and coherent design. With the help of numerical flow simulations, the performance of these designs for both pumps could be predicted with greater accuracy, so that the design could be validated and production launched shortly.

This project enabled me to learn a great deal of knowledge and skills in many fields, including turbo-machinery, a field in which I had no experience and never had the chance to study at EPFL. I was also able to learn how to use open-FOAM in great detail, correcting the errors one by one until the preliminary simulations ran and converged. Although more difficult and time-consuming at first, this software pushed me to understand the theory behind CFD in depth.

Finally, on a personal level, I really enjoyed working on this project and am determined to continue the work over the summer and next year to test and later optimize these pumps. My colleagues and I are also looking into opportunities to publish a paper at a conference on turbo-machinery or space propulsion, such as the 3AF International Conference On Space Propulsion in 2024 in which we plan to participate in.

References

[1] D. Tate Fanning, "A numerical study of the development of inducer backflow," 2017.

[2] Kenneth E. & Nichols P.E., "How to select turbomachinery for your application," 2019, [Online; accessed 07-april-2023].

[3] Johann Friedrich Gülich, *Centrifugal Pumps, Second Edition*, Springer, 2010.

[4] Luca d'Agostino, Angelo Cervone, Lucio Torre, Giovanni Pace, Dario Valentini, and Angelo Pasini, *An Introduction to Flow-Induced Instabilities in Rocket Engine Inducers and Turbopumps*, pp. 65–86, 03 2017.

[5] Jinfeng Zhang, Guidong li, Jieyun Mao, Shouqi Yuan, Yefei Qu, and Jing Jia, "Effects of the outlet position of splitter blade on the flow characteristics in low-specific-speed centrifugal pump," *Advances in Mechanical Engineering*, vol. 10, pp. 168781401878952, 07 2018.

[6] Pranit M. Patil and Rushikesh Todkar, "An overview of effect of splitter blades on centrifugal pump performance," *International journal of engineering research and technology*, vol. 2, 2013.

[7] Alasdair McMullin & Ludovic Chan, "Design of liquid oxygen and ethanol electric pumps for rocket engine," Internal Document, 2022, [Online; accessed 20-june-2023].

[8] Johann Friedrich Gülich, "Selection criteria for suction impellers of centrifugal pumps," *World Pumps*, vol. Volume 2001, Issue 414, 2001.

[9] Doruk Turgul, "Design, construction and performance evaluation of a centrifugal pump for an energy efficient dishwasher," 2015, [Online; accessed 20-march-2023].

[10] M. J. Lubieniecki, "Rocket engine inducer design optimisation to improve its suction performance," 2018, [Online; accessed 07-april-2023].

[11] Francesco Torre, "Design optimization of splitter blades for rocket engine turbopump," 2018, [Online; accessed 07-april-2023].

[12] CFturbo GmbH, "Cfturbo software manual," [Online; accessed 19-may-2023].

[13] ANSYS Inc, "Ansys mechanical user's guide," *Release 17.2.*, 2022.

[14] Engineering ToolBox, ," [Online; accessed 19-may-2023].

[15] The OpenFOAM Foundation, "Openfoam website," [Online; accessed 12-june-2023].

[16] Volupe AB, "y+ compute grid spacing online," [Online; accessed 12-june-2023].

Req. ID	Short	Description	Rationale
PUMP-01	Pump Concept	Each pump shall accelerate, using an electric motor, the propellant of demo B2 engine [LOX & 90 % Purity Ethanol]	
PUMP-02	Pump Inlet Pressure	The inlet pressure shall be 5 [±0.25] bars	6 bars Tanks & Losses
PUMP-03	Pump Outlet Pressure	The outlet pressure shall be 38 [±3.8] bars	25 bars in CC + Losses
PUMP-04	Pump Mass Flow	The outlet mass flow shall be within [±10%] of its nominal value	Margins in the motor performances
PUMP-05	Operation duration	Pumps shall be operable on a duration of at least 10x 10 s without presenting any performance degradation under 95 % of the initial measured performances	Re-usability & ease of testing
PUMP-06	Fluid Interface	All fluid interface in the main line shall be compatible with 1/2" pipes	ERT Standards
PUMP-07	Pump Operations	Operation of each pump shall be independent of the other pump	Ease of development
PUMP-08	Pump Manufacturing	Both pumps should be machinable by NC/conventional machining, *i.e. chips removal*	Backup up of manufacturing
PUMP-09	Fluid Compatibility	Each pump's components shall be chemically compatible with the respective fluid it is in contact with	Prevent degradation & Safety
PUMP-10	Pump Assembly	The pump shall be entirely dismountable by a maximum of 2 persons	Ease to update & inspect
PUMP-11	OP Margins	Designed performances shall have at least 5% of margins over OP point	Margins sim2real
PUMP-12	Cavitation Margins	The cavitation number shall always be above 1 [- 0 ; + 0.2]	Prevent excessive cavitation
PUMP-13	Pump Sealing	The pump sealing shall have a leakage rate below 1% of the nominal outflow rate	Reduces losses

Table 12: Key requirements overview for the electric pumps

B Propellants Properties

Table 13: Physical properties of the propellants used

	Ethanol	**LOX**
Density ρ [kg/m^3]	785	1'152
Operating Temperature T [K]	288	90
Dynamic Viscosity ν [P_a/s]	0.001231	$1.95e^{-4}$
Kinematic Viscosity ν [m^2/s]	$1.60e^{-6}$	$1.71e^{-7}$
Thermal Conductivity λ [W/(m·K)]	0.21	0.15
Heat Capacity c_p [J/(kg·K)]	2'620	1'750
Vapour pressure pv [Pa]	4'020	10'340

C Full Design Reports

Table 14: Key values from CFturbo

	Ethanol	**LOX**
Inlet Stator		
Absolute velocity C_1 [m/s]	8.2	9
Absolute velocity C_2 [m/s]	2.8	3.2
Diameter ratio [-]	2.344	2.303
Width ratio [-]	1.262	1.24
Area ratio [-]	2.959	2.856
Axial extension Δz [mm]	32.5	31.9

	Ethanol	**LOX**
Inducer		
Peripheral velocity u_1 [m/s]	18.7	19.8
Absolute velocity C_1 [m/s]	8.2	3.2
Relative velocity W_1 [m/s]	18.9	20
Relative flow angle β_1 [°]	8.4	9.1
Total outlet pressure $P_{2,total}$ [bar]	6.16	6.98
Peripheral velocity u_2 [m/s]	23.2	24.7
Meridional velocity C_{m2} [m/s]	4	4.7
Circumferential velocity C_{u2} [m/s]	12	12.5
Absolute velocity C_2 [m/s]	12.7	13.4
Relative velocity W_2 [m/s]	11.9	13
Absolute flow angle α_2 [°]	18.6	20.5
Relative flow angle β_2 [°]	19.9	21.1
Work coefficient φ [-]	0.356	0.374
Specific diameter δ [-]	2.486	2.427
Total flow coefficient φ_t [-]	0.097	0.104
Meridional flow coefficient φ_m [-]	0.14	0.154
Meridional velocity ratio [-]	1.453	1.485
Relative velocity ratio [-]	0.833	0.828
Area ratio [-]	0.688	0.673
Stepanoff NPSHR [m]	8.65	10.19
Axial extension Δz [mm]	12.5	12.1
Thickness LE [mm]	0.5	0.3
Thickness TE [mm]	0.5	0.5
LE blade angle β_{B1} [°]	24.1	24.1
TE blade angle β_{B2} [°]	36.8	40
Throat area $[mm^2]$	27.65	22.06
Overlapping	1.674	1.931
Slip coefficient	0.914	0.903

	Ethanol	**LOX**
Centrifugal Impeller		
Peripheral velocity u_1 [m/s]	23.2	24.7
Meridional velocity C_{m1} [m/s]	4	4.7
Circumferential velocity C_{u1} [m/s]	11.9	12.1
Absolute velocity C_1 [m/s]	12.6	13
Relative velocity W_1 [m/s]	12	13.4
Absolute flow angle α_1 [°]	18.7	21.1
Relative flow angle β_1 [°]	19.7	20.5
Total outlet pressure $P_{2,total}$ [bar]	38	38
Peripheral velocity u_2 [m/s]	95.4	74.4
Meridional velocity C_{m2} [m/s]	1.5	2.4
Circumferential velocity C_{u2} [m/s]	91.2	67.6
Absolute velocity C_2 [m/s]	91.2	67.7
Relative velocity W_2 [m/s]	4.5	7.2
Absolute flow angle α_2 [°]	0.9	2.1
Relative flow angle β_2 [°]	19.3	19.8
Work coefficient φ [-]	0.891	0.981
Specific diameter δ [-]	19.83	12.38
Total flow coefficient φ_t [-]	0.002	0.006
Meridional flow coefficient φ_m [-]	0.015	0.033
Meridional velocity ratio [-]	0.365	0.522
Relative velocity ratio [-]	0.372	0.473
Area ratio [-]	2.74	1.915
Stepanoff NPSHR [m]	8.65	10.19
Relative flow angle β_{S0} [°]	4.9	4.9
Axial extension Δz [mm]	7.5	7.5
Thickness LE [mm]	1.1	1.2
Thickness TE [mm]	1.3	1.2
LE max blade angle β_{B1} [°]	37.6	37.6
LE min blade angle β_{B1} [°]	18	18.7
TE max blade angle β_{B2} [°]	44.5	41.5
TE min blade angle β_{B2} [°]	38.2	41.5
Throat area [mm^2]	22.54	26.81
Blade Edge Throat area [mm^2]	24.17	[-]
Main Overlapping	3.5	2.45
Splitter Overlapping	1.07	0.64
Slip coefficient	0.976	0.95

	Ethanol	**LOX**
Volute		
Swirl [m^2/s]	3.466	1.859
Absolute velocity C_2 [m/s]	88.9	65.2
Equivalent diameter D [mm]	5.29	6.39
Side ratio [%]	91.8	95.4
Last spiral Swirl [m^2/s]	1.956	1.122
Last spiral Absolute velocity C_2 [m/s]	47.3	35.6
Cone angle ϑ [°]	4.2	3.9
Velocity ratio [-]	0.173	0.253
Spiral start position $\varphi_{c,0}$ [°]	20.7	22
Cutwater Equivalent diameter D_c [mm]	6.98	7.61
Inner angle α_{in} [°]	4.2	3.3
Outer angle α_{out} [°]	14.9	17.3

D LOX Pump Overview

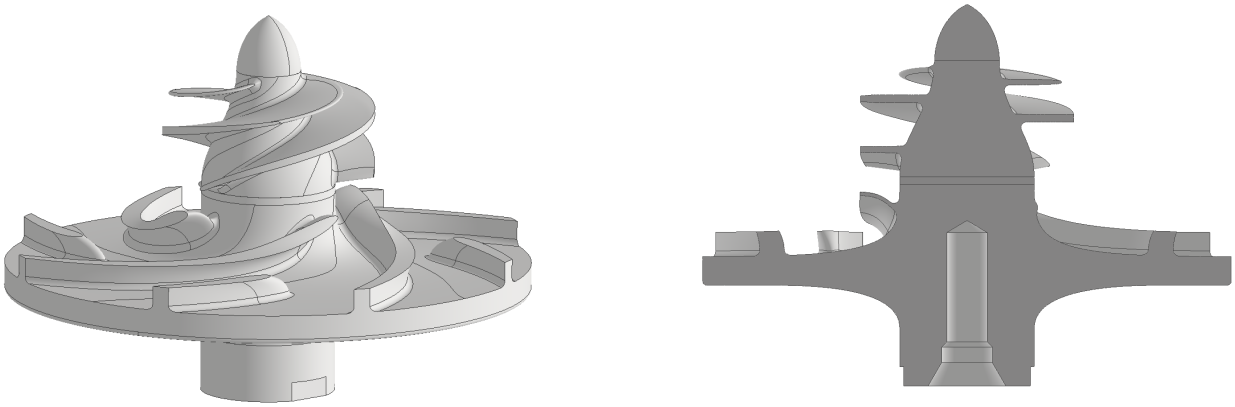

(a) 3D View

(b) Cutaway View

Figure 26: LOX Pump Impeller final design

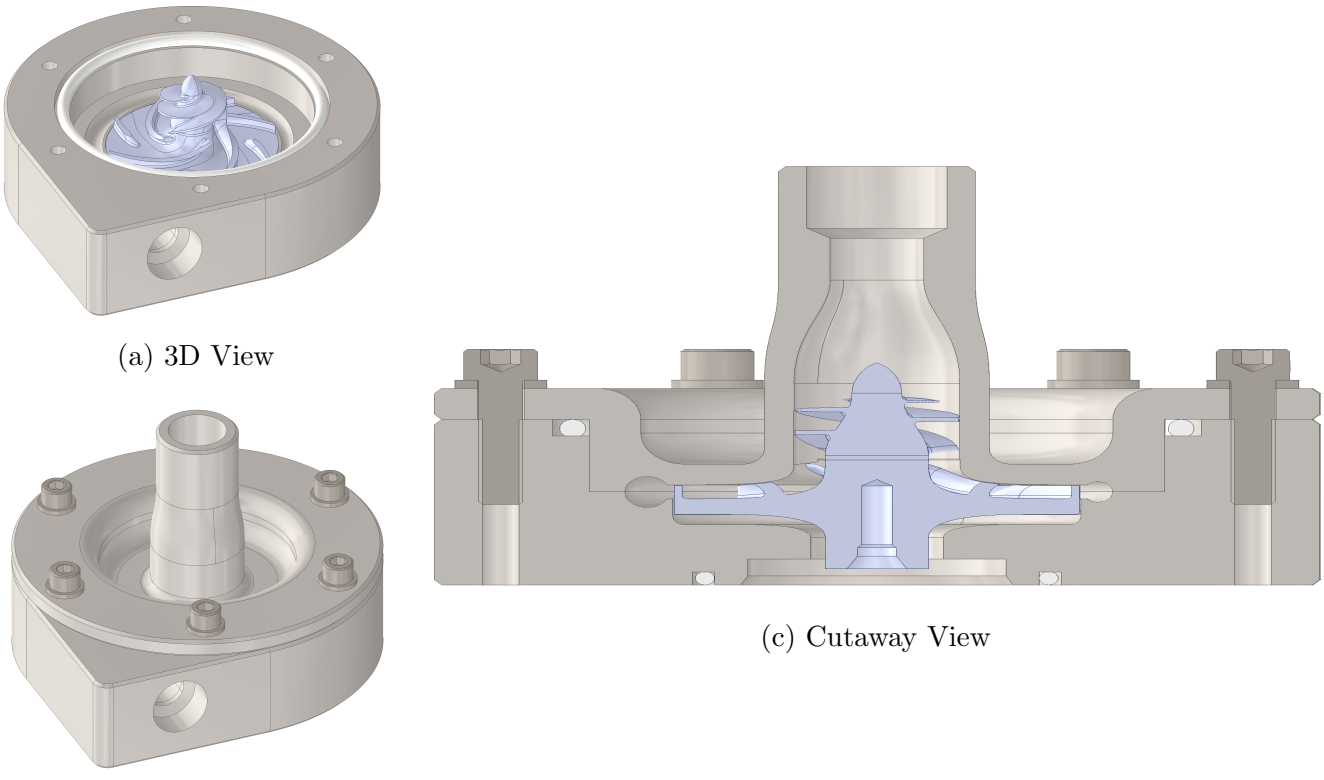

(a) 3D View

(b) 3D View opened

(c) Cutaway View

Figure 27: Lox Pump casing assembly

E Open-FOAM Preliminary simulations

Geometry & Mesh

Preliminary simulations for the Ethanol Pump have been conducted using the open source workflow presented in section 7.1. The full 360° fluid domain has been exported from CFturbo as the starting point of this simulation. This domain has then been split into 4 subdomains as presented in the following list :

- **Inlet**, including the 1/2" inlet extension, the diffuser until the inlet section of the inducer with the cone.
- **Rotating Impeller**, including the inducer stage, the axial stator and the centrifugal impeller stage of the pump.
- **Joints**, including the small outlet extension at the back of the impeller.
- **Volute**, including the volute and the associated stator.

Then, these domains have been imported to the SALOME mesher. The generated mesh used the Netgen algorithm to generate mainly 3d tetrahedral elements with the following table summarizing several mesh metrics :

Table 15: Mesh Metrics

Metrics	**Lowest**	**Average**	**Highest**
Total Number of Nodes		129'759	
Total Number of Faces		1'139'338	
Total Number of Elements		289'605	
Face Area	3.560e-09		1.060e-05
Volume	2.195e-13		8.739e-09
Maximum Aspect ratio		16.53	
Non-orthogonality (1488 cells)		8.569	79.214
Maximum cell openness		2.669	
Maximum Skewness		1.420	
Total Number of Nodes		129'759	
Total Number of Faces		1'139'338	
Total Number of Elements		289'605	

Figure 28: Mesh Generated for the OpenFOAM simulation

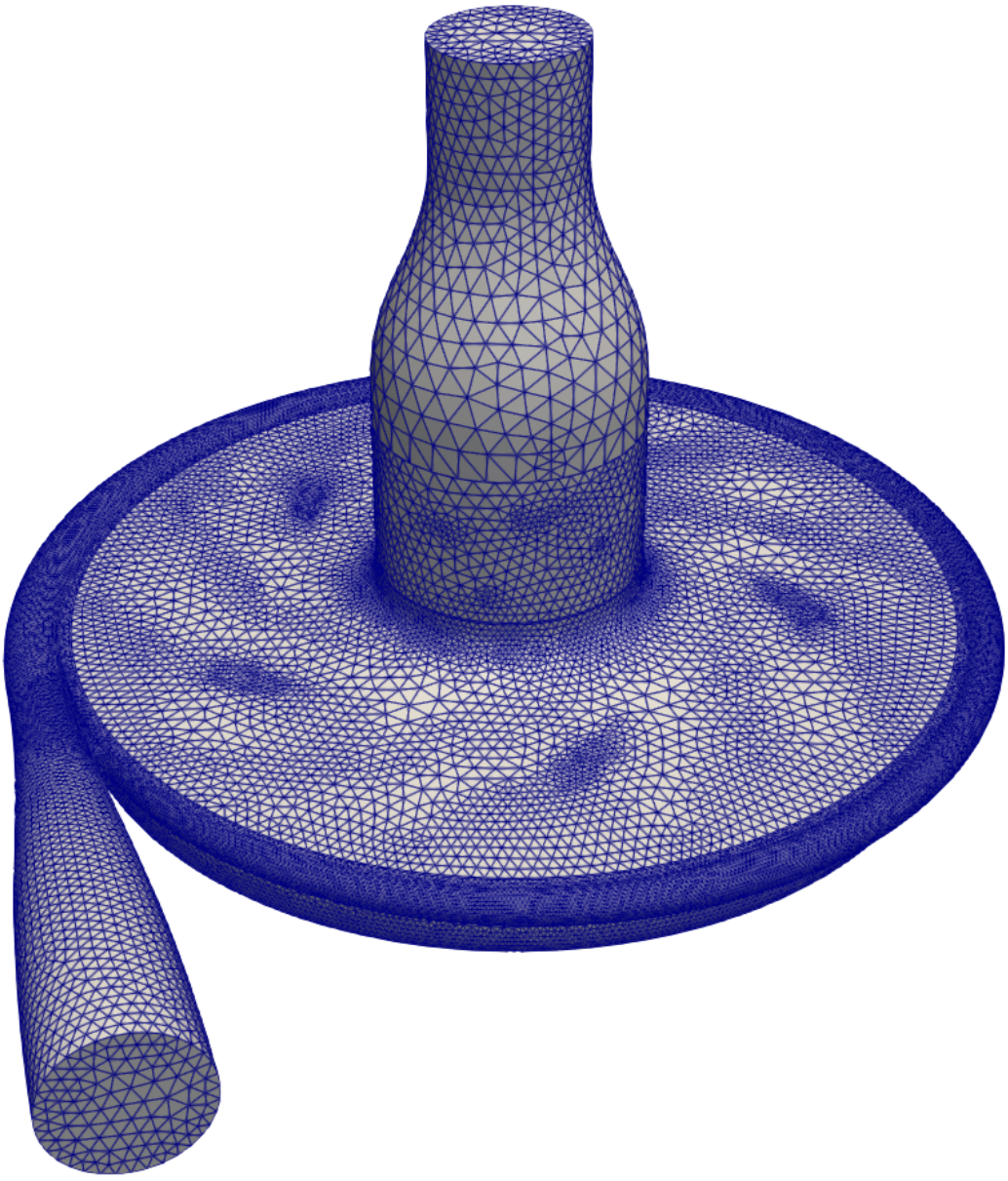

BC & Key parameters

In order to compute the simulation several boundary conditions were applied to the mesh, but first the rotation of the rotating impeller subdomain is implemented using the Multiple Reference Frame method.

Then , the following boundary conditions were introduced :

- At the Inlet, a total pressure of 5 bars *(using "totalPressure" type)* supported with a "inletOutlet" type for velocity to prevent back-flow and ease the convergence.
- At the Volute outlet, the flow rate is forced to its nominal value of 0.001039 $[m^3/s]$(using "flowRateOutletVelocity") with a zero gradient condition on the pressure field.
- Similarly, at the Joint outlet, the flow rate is forced to its maximal value of 0.00001039 $[m^3/s]$(using "flowRateOutletVelocity") with a zero gradient condition on the pressure field.
- Impeller's walls as well as casing's wall boundary condition were defined as no slip walls with zero gradient condition on the pressure.
- Finally, patches joining at each subdomains have been duplicated to create a cyclic boundary condition as only the topology matches and not the mesh.

Table 16 presents all the other key values used in our simulation.

Table 16: Key values used in OpenFOAM

	Value used
Turbulence Model	k - ω
k $[m^2/s^2]$	0.25318
Wall surface roughness R_a [μ m]	1.6
ω $[s^{-1}]$	15823.63
time-step Δt [s]	0.00005
End time t_{end} [s]	0.5
Solver	simpleFoam
Velocity solver	GAMG
Other quantities Solver	Gauss smoothSolver
Tolerance	1e-16;

One can not that using the steady-state incompressible fluid solver simpleFoam, the pressure has to be defined as the specific pressure (pressure divided by fluid density). Moreover, as the mesh features a several non orthogonal cells, the NonOrthogonalCorrector is activated with low relaxation factors (0.1 and 0.2 for pressure field only).

Results & Post-processing

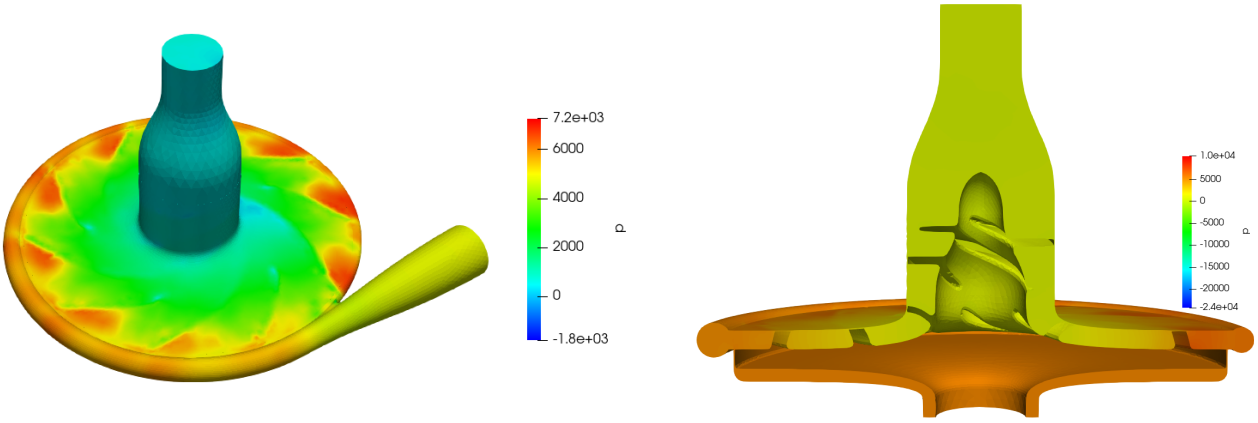

(a) 3D View (b) Cutaway View

Figure 29: Specific pressure field at final time

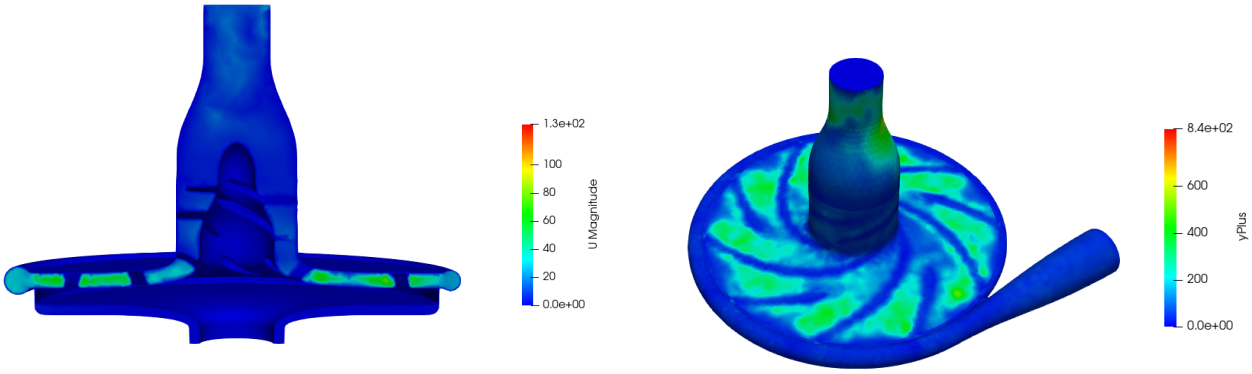

(a) Velocity magnitude cutaway view (b) yPlus 3D view

Figure 30: LOX Pump Impeller final design

As seen on table 17, the preliminary are already quite close to what was expected. However, simulation could have run longer to achieve better convergence. Impeller forces and torque couldn't be extracted due to the MRF setup and the way patches had been defined. Finally, the lack of inflation layer near the walls lead to high yPlus values that is also a cause in some imprecise results obtained (Vorticity field at joint outlet for example).

Table 17: Numerical results of the Preliminary simulations

	Value
yPlus [-]	
Minimum	4.09
Average	84.72
Maximum	1'907.64
Residuals	
p	3.9e-03
u_x	9.34e-05
u_y	9.83e-05
u_z	3.012e-04
Operating Point	
Outlet total pressure p_{tot} [bars]	35.191
Joint Outlet	
Total pressure p_{tot} [bars]	39.611
Vorticity $[s^{-1}]$	[9.574 ; 49.61 ; 95.71]

F LOX Pump Mesh Visualisation

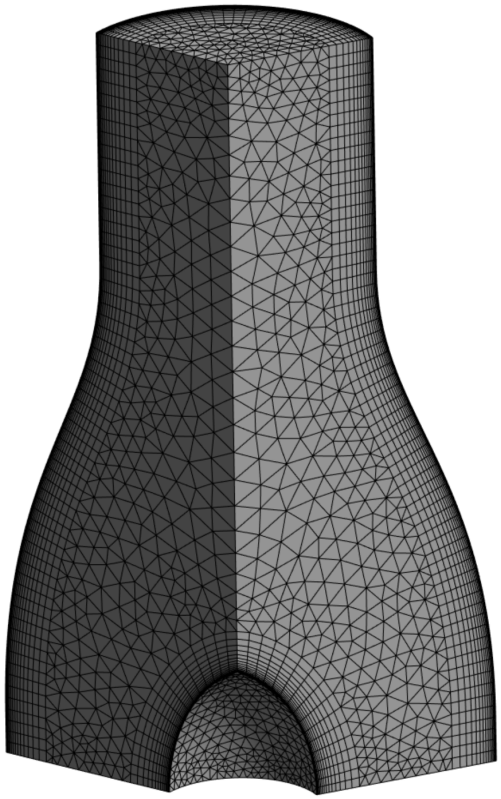

(a) 3D View of the Inlet extension mesh

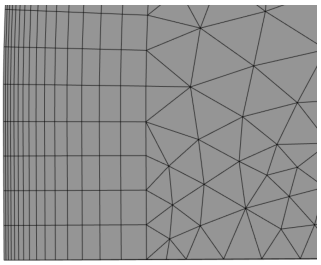

(b) Inflation Layer detail

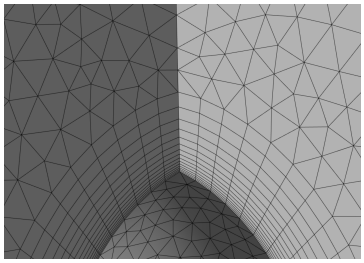

(c) Top of Cone detail

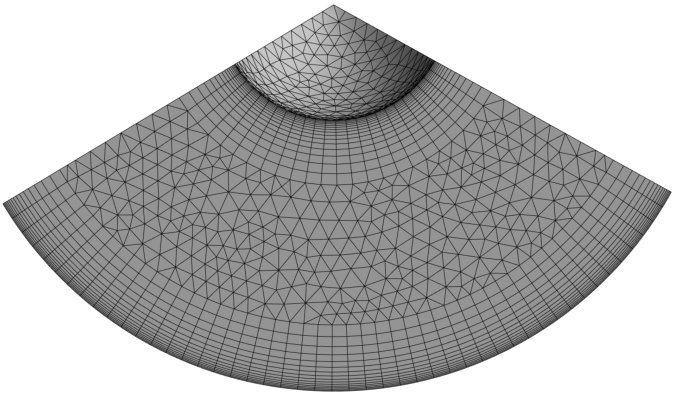

(d) Back of the Inlet extension View

Figure 31: Generated Mesh for the Inlet extension domain of the LOX pump

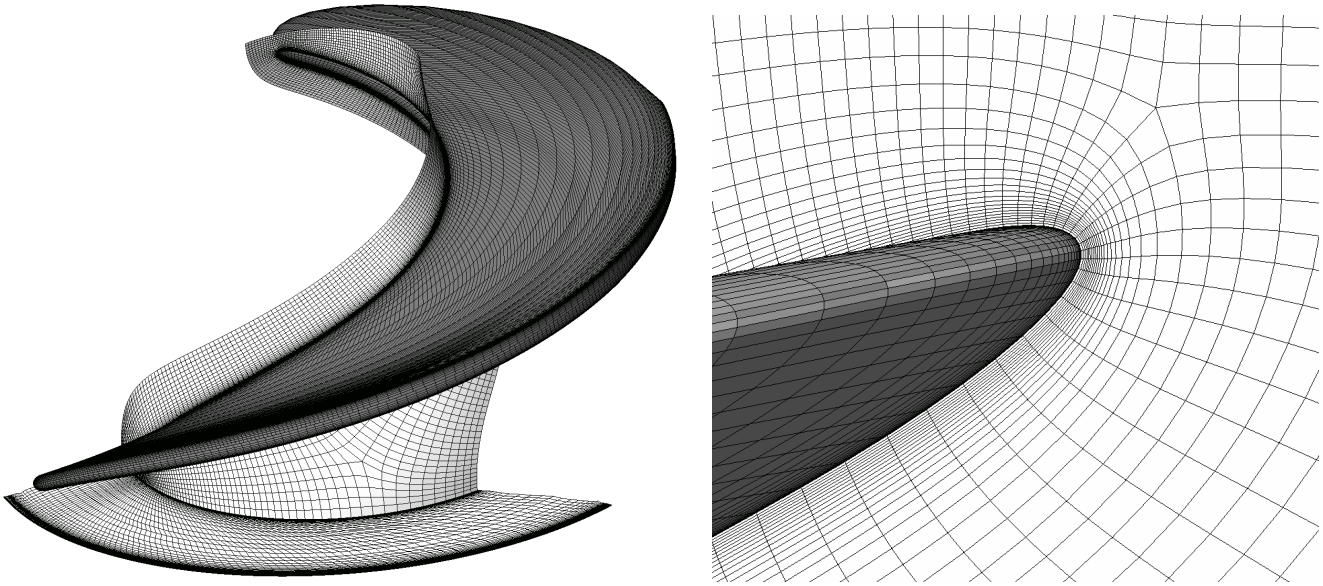

(a) 3D View

(b) Leading Edge Hub detail

Figure 32: Generated Mesh for the Inducer of the LOX Pump

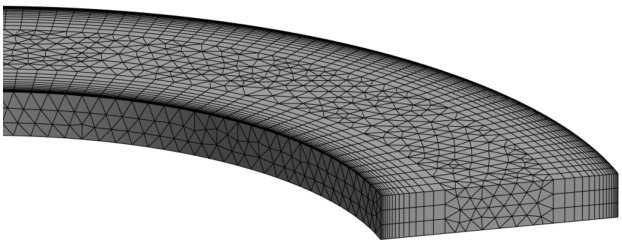

Figure 33: Generated Mesh for the Axial stator domain of the LOX Pump

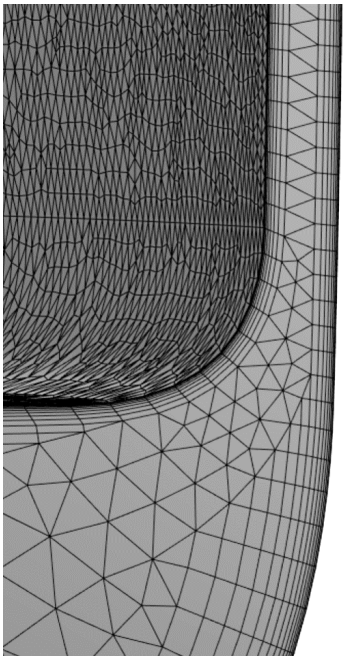

(a) Inflation Layer detail

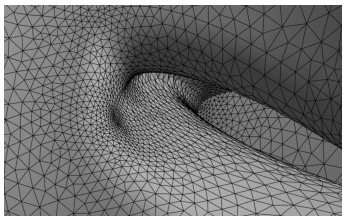

(b) Main Blade LE detail

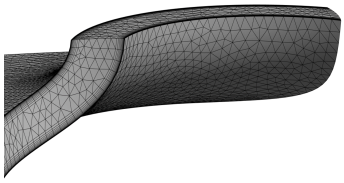

(c) Leakage Outlet detail

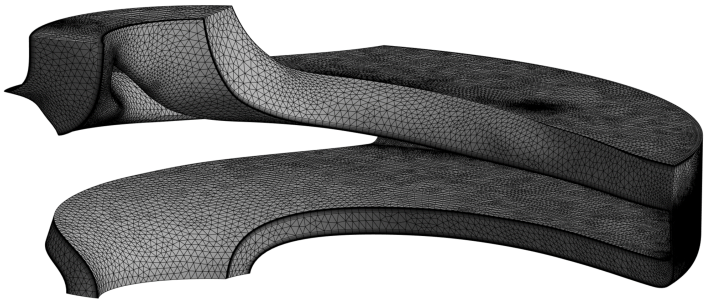

(d) 3D View

Figure 34: Generated Mesh for the Impeller domain of the LOX Pump

(a) 3D View

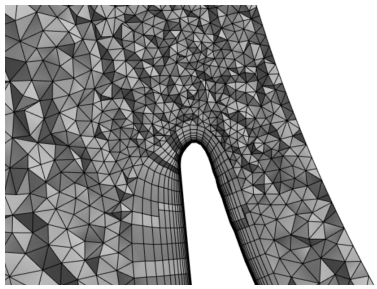

(b) Cut-water Cutaway detail

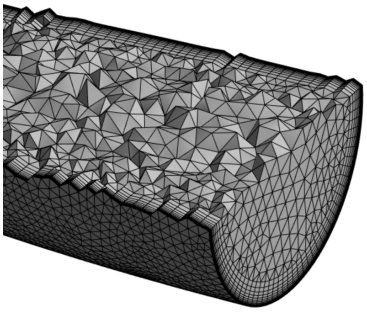

(c) Outlet Cutaway detail

Figure 35: Generated Mesh for the Volute domain of the LOX pump